INSTITUTO POLITÉCNICO NACIONAL

Centro de Investigación en Ciencia Aplicada y Tecnología

Avanzada Unidad Legaria

CICATA-IPN Legaria

Evaluation of Hexacyanoferrates as cathode for Rechargeable Sodium Ion Batteries

T HE S I S

Of a thesis submitted in partial fulfillment of the requirements

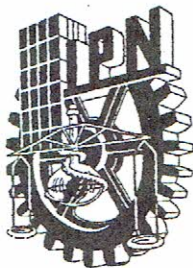for the Doctor in Advanced Technology degree

By

Miguel Angel Oliver Tolentino

Thesis Supervisor: Prof. Edilso Reguera Ruiz

Mexico City; May, 2017.

INSTITUTO POLITÉCNICO NACIONAL
SECRETARÍA DE INVESTIGACIÓN Y POSGRADO

CARTA CESIÓN DE DERECHOS

En la Ciudad de _México_ el día __25__ del mes ___04___ del año _2017_, el (la) que suscribe___Miguel Angel Oliver Tolentino_____ alumno (a) del Programa de__ Doctorado en Tecnología Avanzada__ con número de registro _B130166___, adscrito al _Centro de Investigación en Ciencia Aplicada y Tecnología Avanzada Unidad Legaria CICATA-Legaria_, manifiesta que es autor (a) intelectual del presente trabajo de Tesis bajo la dirección de _Dr. Edilso Francisco Reguera Ruiz___ y cede los derechos del trabajo intitulado _ Evaluation of Hexacyanoferrates as cathode for Rechargeable Sodium Ion Batteries _, al Instituto Politécnico Nacional para su difusión, con fines académicos y de investigación.

Los usuarios de la información no deben reproducir el contenido textual, gráficas o datos del trabajo sin el permiso expreso del autor y/o director del trabajo. Este puede ser obtenido escribiendo a la siguiente dirección _maoliver@ipn.mx___. Si el permiso se otorga, el usuario deberá dar el agradecimiento correspondiente y citar la fuente del mismo.

Miguel Angel Oliver Tolentino
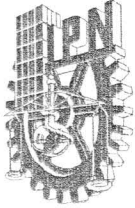
INSTITUTO POLITÉCNICO NACIONAL
SECRETARÍA DE INVESTIGACIÓN Y POSGRADO

ACTA DE REVISIÓN DE TESIS

En la Ciudad de _____ México _____ siendo las __ 13:00 __ horas del día __ 25 __ del mes de _____ Abril _____ del _ 2017 _ se reunieron los miembros de la Comisión Revisora de Tesis, designada por el Colegio de Profesores de Estudios de Posgrado e Investigación de _____ CICATA-Legaria _____ para examinar la tesis titulada:

Evaluation of Hexacyanoferrates as cathode for Rechargeable Sodium Ion Batteries

Presentada por el alumno:

Oliver	Tolentino	Miguel Angel
Apellido paterno	Apellido materno	Nombre(s)

Con registro: | B | 1 | 3 | 0 | 1 | 6 | 6 |

aspirante de:

Doctorado en Tecnología Avanzada

Después de intercambiar opiniones, los miembros de la Comisión manifestaron *APROBAR LA DEFENSA DE LA TESIS*, en virtud de que satisface los requisitos señalados por las disposiciones reglamentarias vigentes.

LA COMISIÓN REVISORA

Director de tesis

Dr. Edilso Francisco Reguera Ruíz
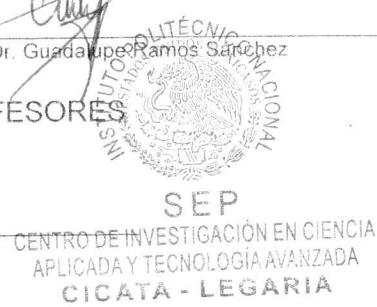
Dr. Miguel Ángel Aguilar Frutis

Dr. Fernando Trejo Zarraga

Dra. Elsa Miriam Arce Estrada

Dr. Guadalupe Ramos Sánchez

PRESIDENTE DEL COLEGIO DE PROFESORES

Dra. Mónica Rosalía Jaime Fonseca

SEP
CENTRO DE INVESTIGACIÓN EN CIENCIA
APLICADA Y TECNOLOGÍA AVANZADA
CICATA - LEGARIA

ABSTRACT

In present work, the open framework materials knows as hexacyanoferrate were studied as cathode in sodium ion batteries in aqueous and non-aqueous media. In that sense two system were evaluated i) the Zinc Hexacyanoferrate as building block, where iron is found in low spin with octahedral coordination and zinc has tetrahedral coordination. The $Na_2Zn_3[Fe(CN)_6]_2 \cdot zH_2O$ exhibited a low stability in aqueous media during redox process, however, the effect of compensation cation (K^+, Rb^+ and Cs^+) within structure over the electrochemical performance in sodium aqueous solution revealed that K^+ and Rb^+ are progressively displaced by the sodium ion, which was ascribed to its higher mobility. But, when the experiment is conducted using Cs^+, the mixed composition, $Zn_3NaCs[Fe^{II}(CN)_6]_2 \cdot zH_2O$ is formed, enhancing their charge retention around to 75% during 40 charge/discharge cycles. Whereas, in non-aqueous media, the system exhibited two different mechanisms of sodium insertion/desertion; the dehydrated form of zinc hexacyanoferrate $Na_2Zn_3[Fe(CN)_6]_2$, revels a better rate capacity retention, due to higher mobility of sodium inside the structure. On the other hand, ii) the Manganese Hexacyanoferrate $Na_{2y}Mn[Fe(CN)_6]_y \cdot zH_2O$ as building block where iron is found low spin and manganese has octahedral coordination. This material is unstable for charge/discharge process due to the Jean Teller distortion present in Mn^{3+}, so that the manganese partial substitution by other $3d$ metal was analyzed, first with cobalt with different Mn/Co ratios. The samples were evaluated in aqueous media, showed that material with (Mn/Co) =1 ($Na_{2y}Mn_xCo_{1-x}[Fe(CN)_6]_y \cdot zH_2O$) has the better electrochemical performance, with a stability similar to obtained for $Na_{2y}Co[Fe(CN)_6]_y \cdot zH_2O$, due to the interaction between Mn and Co in the framework, which occurs by spin delocalization. From these results, the materials with similar atomic ratios where synthetized using Ni and Fe, and were studied in non-aqueous media. In these cases, the stability during redox process follows the order: Fe>Co>Ni, which is associated to the metal polarizing power ability and, in consequence, with different charge subtraction capacity and, from this fact, inducing certain spin delocalization and Jahn Teller effect.

Resumen

En el presente trabajo, se estudiaron los materiales como Hexacianoferrato como cátodo en baterías de ion sodio en medios acuosos y no acuosos. En ese sentido, dos Sistema fueron evaluados i) el Zinc Hexacianoferrato como bloque de construcción, donde se encuentra el hierro en bajo spin con coordinación octaédrica y el zinc tiene coordinación tetraédrica. Los $Na_2Zn_3[Fe(CN)_6]_2 \cdot zH_2O$ mostraron una baja estabilidad en medios acuosos durante el proceso redox, sin embargo, el efecto de catión de compensación (K^+, Rb^+ Y Cs^+) dentro de la estructura, sobre el comportamiento electroquímico en solución una solución acuosa de Sodio, reveló que el K^+ y Rb^+ son desplazado progresivamente por el ion sodio, atribuido a su mayor movilidad, pero cuando el experimento se realiza usando Cs^+, se obtiene la composición mixta, $Zn_3NaCs[Fe^{II}(CN)_6]_2 \cdot zH_2O$, aumentando su retención de carga en torno al 75% durante 40 ciclos de carga / descarga.

Mientras que en medios no acuosos, este material presenta dos diferentes mecanismos de inserción/deserción de sodio; la forma deshidratada de zinc Hexacianoferrato $Na_2Zn_3[Fe(CN)_6]_2$, revela una mejor retención de la capacidad tarifaria, debido Movilidad del sodio dentro de la estructura. Por otro lado, ii) el manganeso hexacianoferrato $Na_{2y}Mn[Fe(CN)6]_y \cdot zH_2O$ como bloque de construcción donde el hierro bajo spin y el manganeso alto spin tiene coordinación octaédrica. Este material es inestable para carga/descarga debido a la distorsión de Jean Teller presente en Mn^{3+}, de manera que la sustitución parcial de manganeso por otro metal 3d fue estudiada, primero con cobalto a diferentes relaciones Mn/Co. Las muestras fueron evaluadas en medio acuoso, mostrando que el material con (Mn/Co)= 1 ($Na_{2y}Mn_xCo_{1-x}[Fe(CN)_6]_y \cdot zH_2O$) tiene el mejor comportamiento electroquímic, con una estabilidad similar a la obtenida para $Na_{2y}Co[Fe(CN)6]_y \cdot zH_2O$, debido a la interacción entre Mn y Co en la estructura, que se produce por la deslocalización de spin.

A partir de estos resultados, los materiales con relaciones atómicas similares donde se sintetizaron usando Ni y Fe, y se estudiaron en medios no acuosos. En estos casos, la estabilidad durante el proceso redox es en el orden siguiente: Fe> Co> Ni, que se asocia al poder polarizante del metal y en consecuencia, con diferente capacidad de sustracción de carga lo que permite modular la deslocalización de spin y el efecto Jahn Teller.

Acknowledgment

"The true lover of life is the scientist, because, he is the only one who
It deals with discovering its mysteries".

I wat to dedicate this thesis, firstly to my parents for his teachings and example about the dedication, work and effort that one must do to achieve his goals. To my brother for your support throughout this stage of my life. To Dr. Edilso for all his teachings and for giving me the opportunity and confidence to carry out this research project. To Ariel for his academic and personal support.

To my collage of CICATA as: Adela, Lorena, Juvencio, Marlene, Manuel, Monica, Abel Lichi, Nelly and Cuco who always helped me when I needed it. To Drs. Rosa, Daniel, Jorge, Arturo, Itzia, Olivia, Sandra, Guadalupe and Ignacio, who gave me the opportunity to collaborate in different projects and that, I am sure that we will continue doing.

INTRODUCTION

The increase in the use of technologies to obtain energy from renewable sources is closely related to social, economic and political problems. The efforts in such sense are dominated by the availability of appropriate materials to make possible the processes of energy conversion and storage. The energy storage is probably the main challenge for a massive introduction of renewable energy in the national and global energetic matrix. The sources of renewable energy have time fluctuating character, with mismatching between availability and demand related to their seasonal dependence, sequence of days and nights, and to changes in the climate. For instance, the hours of higher solar radiation not necessarily coincide with those of higher demand of electric energy. Such mismatching explains the necessity of energy harvesting and its storage in order to satisfy the demand when it exceeds the generation capacity. In this field, the batteries have proved to be the most promising energy storage devices, however they still present problems of stability, reason why the design and synthesis of materials that have a great stability during the redox cycles is one of the priority of research and innovation.

In this context, this work is based on the study the open framework materials know as Prussian blue analogues (PBA) or Hexacyanometallates as cathode for Sodium Ion Batteries (SIB). The text is divide in four chapter, in the chapter 1 the state of the art is discussed, shown interesting data on energy storage needs, the use of lithium ion batteries, and from the national and global availability of Li, the need to use another type of alkaline ion, disposable and with acceptable mobility. Later, the current state of the art

on materials for anodes and cathodes, especially the use of PBA as cathodes is discussed and the related strategies that have been reported to improve their energy storage capacity, chemical and thermal stabilities and under cycles of charge/discharge (cyclability).

The chapter 2 discusses the experimental procedures used, which include the materials synthesis methods, samples characterization, and electrochemical studies. Chapters 3 and 4 discuss the results concerning to the behavior of zinc hexacyanoferrate and manganese hexacyanoferrate in aqueous and non-aqueous media as cathode materials for sodium ion batteries. The results herein discussed are supported by a paper published in Royal Society Advanced (RSC Adv., 2016, 6, 108627) and two additional manuscript already prepared to be submitted for publication.

Index

Content

CHAPTER 1.

1. Introduction

The unlimited increase of the world population has brought to an increase in the demand of electrical energy to satisfy the current needs, so that, energy production and storage, a related materials, appear as the main support as one of the mains supports our society, and their importance increases.

The worldwide electricity demand is predicted to double by the middle of the current century and it will be triplicate by the end of 2100´s. Currently, the worldwide electric generation capacity is estimated to be about 20 terawatt hour[1]. Approximately 68% of today's electrical energy is supplied from fossil fuels: coal (42%), natural gas (21%), oil (5%), nuclear (14%), hydro (15%), and the remaining 3% from renewable energy technologies. The uses carbon derived compounds for energy production has provoked environment problem due to CO_2 emission, a greenhouse gas that is widely considered as the primary contributor to global warming[2]. So those, a variety of renewable and clean energy sources, such as the wind and sun, are growing rapidly.

The solar radiation energy received by Earth 1 h is enough to meet worldwide energy requirements for a year. Capturing a small percentage of potential wind energy could also contribute significantly to meeting the world's electrical energy requirements. While advances in technology are still needed to harvest renewable energy economically, solar and wind power technologies have grown quickly[3].

Nevertheless, the decline in the prices of fossil fuels and the new policies of the present governments especially in United States of America can cause an accelerated decrease in the research related to renewable energy[4]. In this context, Mexico has an enormous capacity to produce renewable energy, especially from solar radiation and wind (see Fig. 1A). In addition, the national policies, at least that is declared, contemplate an increase for the use of renewable energy until reach an 25% on 2027, and to contribute to national energy demand (Fig. 1B).
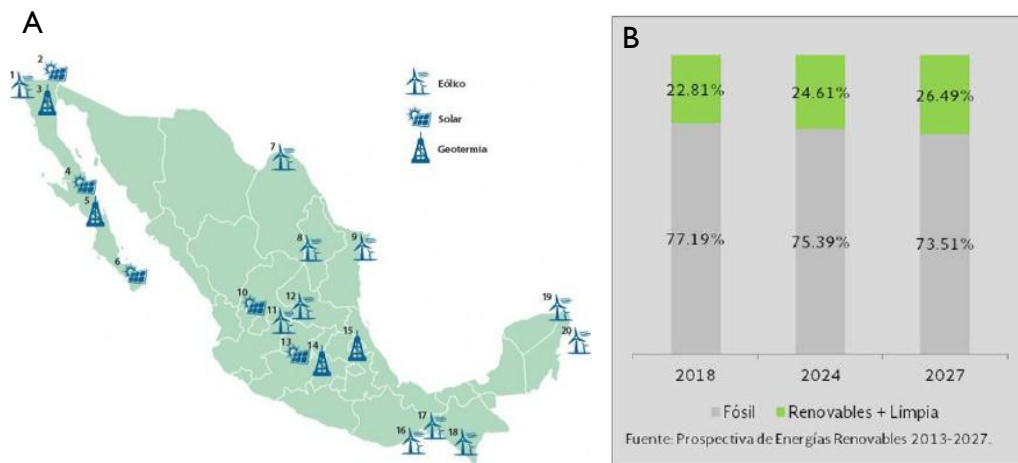
Figure 1. A) Renewable Energy Map and B) Energy production goals in Mexico.

However, solar and wind are not constant and reliable sources of power, so that, the increasing use of renewable energy sources also brings other problems, such as modulating variable renewable resources from time to time and integrating them into the grid smoothly and safely. Balancing electricity generation and demand between daytime and nighttime is also important to optimize grid utilization. Thus, a large-scale stationary energy storage systems (ESSs) connected to renewable power plants have become key

enablers of improving power reliability and quality as well as taking full advantage of high penetration of renewable energy sources[5].

This ESS is an established, valuable approach for improving the reliability and overall use of the entire power system (generation, transmission, and distribution [T&D]). Sited at various T&D stages (Figure 2), ESS can be employed for providing many grid services, including a set of ancillary services such as (1) frequency regulation and load following (aggregated term often used is balancing services), (2) cold start services, (3) contingency reserves, and (4) energy services that shift generation from peak to off-peak periods. In addition, it can provide services to solve more localized power quality issues and reactive power support[2].
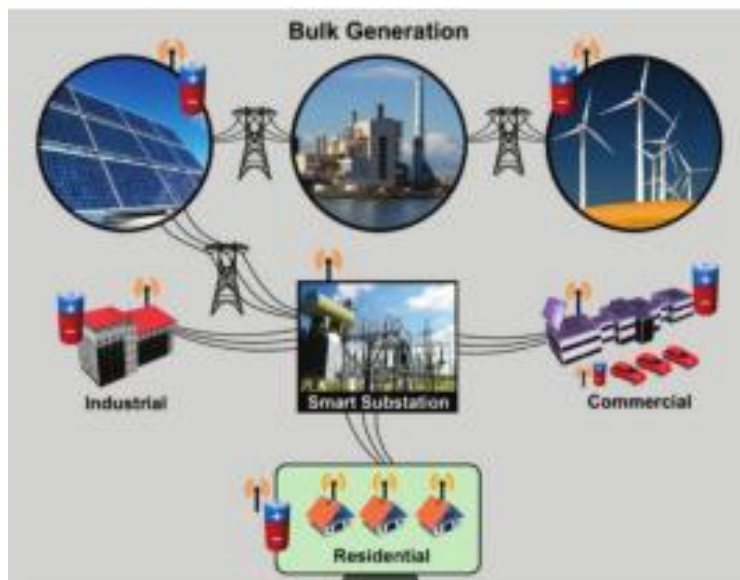

Figure 2. Schematic of applications of electricity storage for generation, transmission, distribution, and end customers and future smart grid.

Balancing services are used to balance generation and demand in tightly limited situations to maintain the alternating current (AC) system frequency of 60 Hz. EES is perfectly suited to provide this service by absorbing electric energy (charging cycle) whenever there is too much generation for a given demand and by injecting electric energy into the power grid (discharging cycle) when there is too little generation[1].

Essential criteria required for large-scale ESSs are: (i) low costs of construction and maintenance, (ii) low risk of safety incidents for long-term utilization, (iii) high round-trip efficiency, and (iv) long cycle life. In addition, environmental benign and nontoxicity should be considered [8]. A number of potential technologies has been proposed for energy storage, among them pump hydro, compressed air, flywheel and electrochemical batteries[6]. Among various energy storage technologies, the secondary battery technique is one of the most promising means for storing electricity on a large-scale because of flexibility, high-energy conversion efficiency and simple maintenance[7].

The most common rechargeable battery systems are lithium ion batteries (LIBs), which consisting of two lithium insertion electrodes and lithium-ion conducting electrolyte, free from lithium metal, have become successful and sophisticated energy storage devices since Sony announced the first version of commercialized lithium (Li)-ion battery (LIB) in 1991, which was a carbon//$LiCoO_2$ cell (Figure 3). This system has rapidly penetrated into everyday life. Compared to other types of rechargeable battery systems, LIB exhibits superb performances in terms of energy density[8].
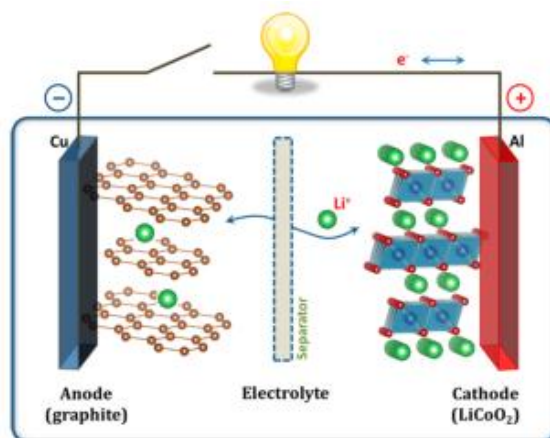
Figure 3. Schematic illustration of the first Li-ion battery ($LiCoO_2$/ Li^+ electrolyte/graphite).

LIBs were originally developed as a high-energy power source for portable electronic devices, and their energy is typically limited to less than 100 Wh as a single battery pack. Cobalt/nickel-based layered materials are often used as positive electrodes for the high energy but small-sized batteries.

LIBs with electric motors are now used as an alternative power source for combustion engines with a fuel tank; (plug-in hybrid) electric vehicles equipped with large-scale LIBs as power sources have been introduced to the automotive market, which could reduce the energy dependence on fossil fuels for a transportation system in the future. The energy of a battery module is increased to 5000–20 000 Wh for (plug-in hybrid) electric vehicles (EVs).

To reduce the battery cost, high-energy cobalt-based materials as positive electrodes cannot be used for large-scale application. In addition, recently, the demand for advanced energy storage technology is rapidly emerging throughout the world. A large-scale energy storage system for the grid is necessary to utilize electrical energy with high efficiency and

for peak shift operation. Indeed, some battery companies have already developed LIBs with megawatt hour (MWh) scale and plan to begin a demonstration test for electrical energy storage (EES)[9].

Such MWh-class batteries are also probably used to store electricity generated from solar cells and wind turbines as green and renewable energy resources. Although LIBs potentially provide a solution to meet these tough challenges to realize sustainable energy development through the increasing market for electric vehicles and an emerging market for EES, we must reconsider the feasibility of lithium, which is certainly the inherent element in LIBs. Lithium is widely distributed in the Earth's crust but is not regarded as an abundant element. The relative abundance of lithium in the Earth's crust is limited to be only 20 ppm as shown in Figure 4. Indeed, the materials cost (the price of Li_2CO_3) was steeply increased during the first decade of this century[10]. Moreover, lithium resources are unevenly distributed (mainly in South America); therefore, production of LIBs depends on the import of lithium from South America.
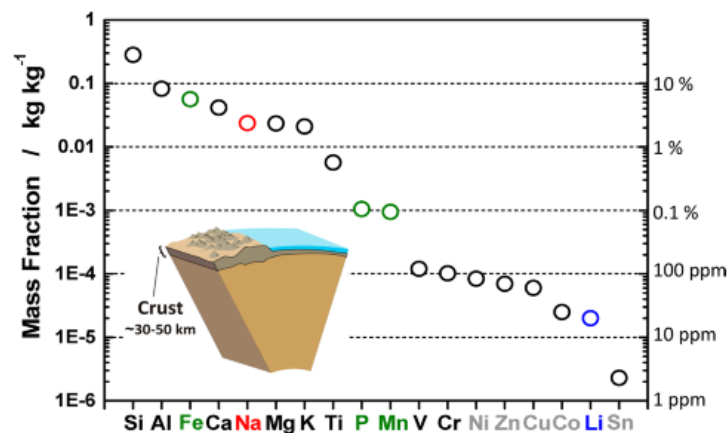
Figure 4. Elemental abundance in the Earth's crust.

In contrast to lithium, sodium resources are unlimited everywhere, and sodium is one of the most abundant elements in the Earth's crust (see Fig. 4). The infinite sodium resources are also found in the ocean[11].

In addition, Mexico offers 11.5% saving in manufacturing costs for the advanced batteries industry compared with other countries (Figure 5) and is the 7th place in NaCl production around the world, so the research and development in this type of storage technologies may be an option that will allow Mexico to become an exporter of these devices.

Advanced Batteries (Green energy)
International Results, 2014 (USA=100.0)

Country	Cost Index
Mexico	93.1
Canada	96.1
Netherlands	97.4
United Kingdom	97.7
Japan	98.3
France	98.5
USA	100.0
Australia	101.2
Germany	101.7
Italy	102.5

Cost Index
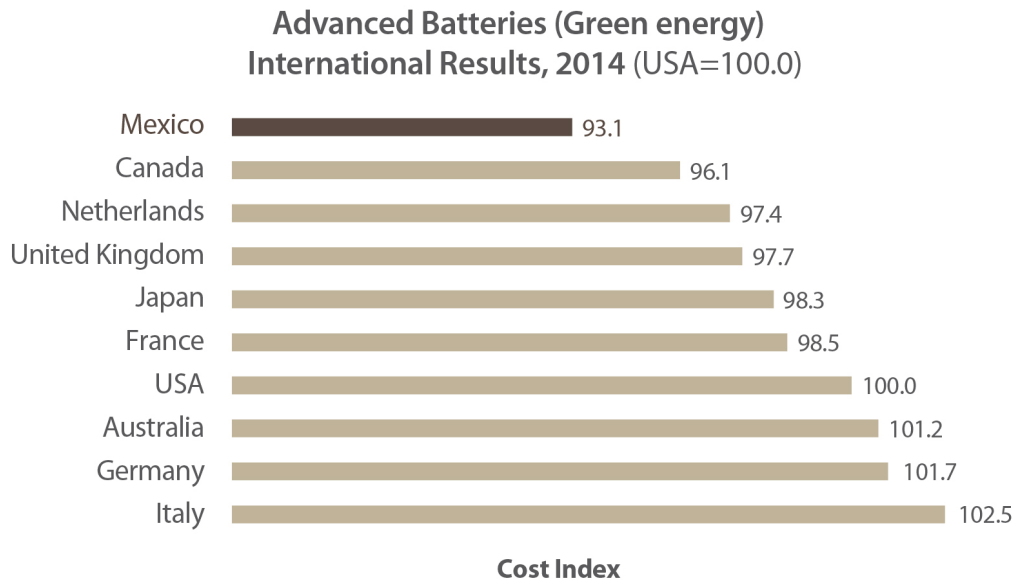
Source: Competitive Alternatives, KPMG's guide to international business location 2014 Edition.

Figure 5. Competitive Alternatives to batteries manufacture.

Sodium is the second-lightest and –smallest alkali metal next to lithium as shown in Table1.

Table 1. Comparison of Physical Properties for Lithium and Sodium

	Na	Li
Cation radius/pm	97	68
Atomic Weight/ g mol^{-1}	23	6.9
E°/ V vs NHE	-2.7	-3.04
A-O coordination	Octahedral or prismatic	Octahedral or tetrahedral
Melting point/ °C	97.7	180.5
Abundance/ mg kg^{-1}	23.6 x 10^3	20
Distribution	Everywhere	70% South America
Price, Carbonates/ USD per kg	~0.32	~6.4

NIBs are operable at ambient temperature, and metallic sodium is not used as the negative electrode, which is different, from commercialized high-temperature sodium-based technology, e.g., Na/S and Na/NiCl batteries[5]. These batteries utilize alumina-based solid (ceramic) electrolyte, and high-temperature operation (~300 °C) is required for maintaining the electrodes in the liquid state to ensure good contact with the solid–electrolyte. Since molten sodium and sulfur are used as active materials at such high temperature, safety issues of these batteries have not been completely satisfied for consumer appliances. In contrast, NIBs consist of sodium insertion materials with aprotic solvent as electrolyte and, therefore, are free from metallic sodium unless there are unfavorable reactions (e.g., overcharge) causing the failure in batteries[12]. Structures,

components, systems, and charge storage mechanisms of NIBs are essentially the same except that lithium ions are replaced with sodium ions as shown in Figure 6.

A NIB consists of two sodium insertion materials, positive and negative electrodes, which are electronically separated by electrolyte (in general, electrolyte salts dissolved in aprotic polar solvents) as a pure ionic conductor[13]. The battery performance depends on battery components selected, and many different NIBs for different purposes can be assembled.
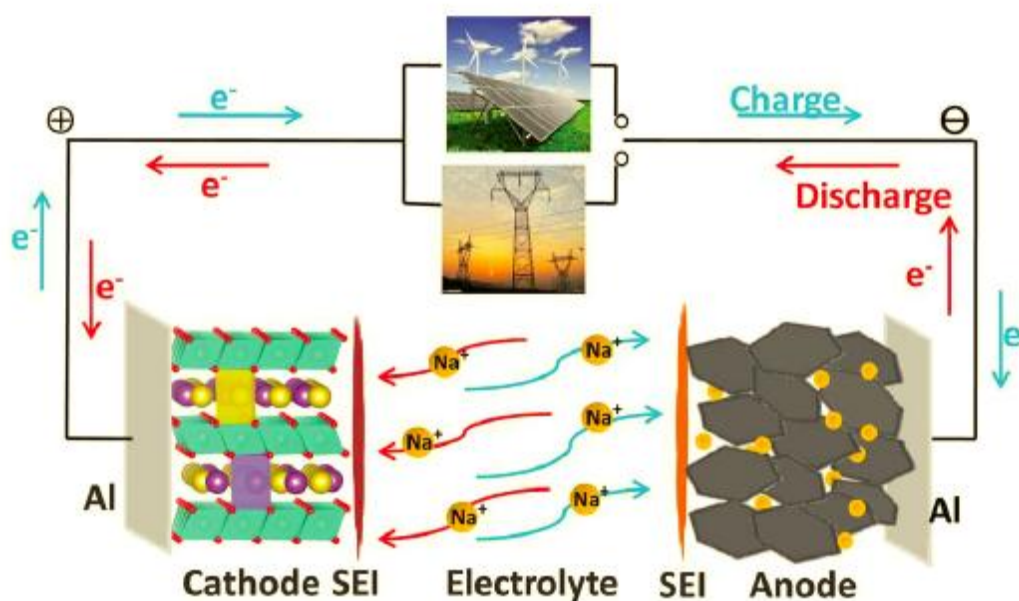
Figure 6. Schematic illustration of Na-ion batteries.

Currently, researches about Na-ion battery has increased in recent years (Figure 7), and are focused on the development of new electrode materials (cathode and anode) and new stable electrolytes (liquid and solid)[7].

For this purpose, fundamental scientific questions need to be further elucidated including:

(1) the difference in transport and kinetic behaviors between Na and Li in analogous

electrodes; (2) Na insertion/extraction mechanism; (3) solid electrolyte interphase (SEI) layer on the electrodes from different electrolyte systems; and (4) charge transfer in the electrolyte-electrode interface and Na$^+$ ion transport through the SEI layer[14].
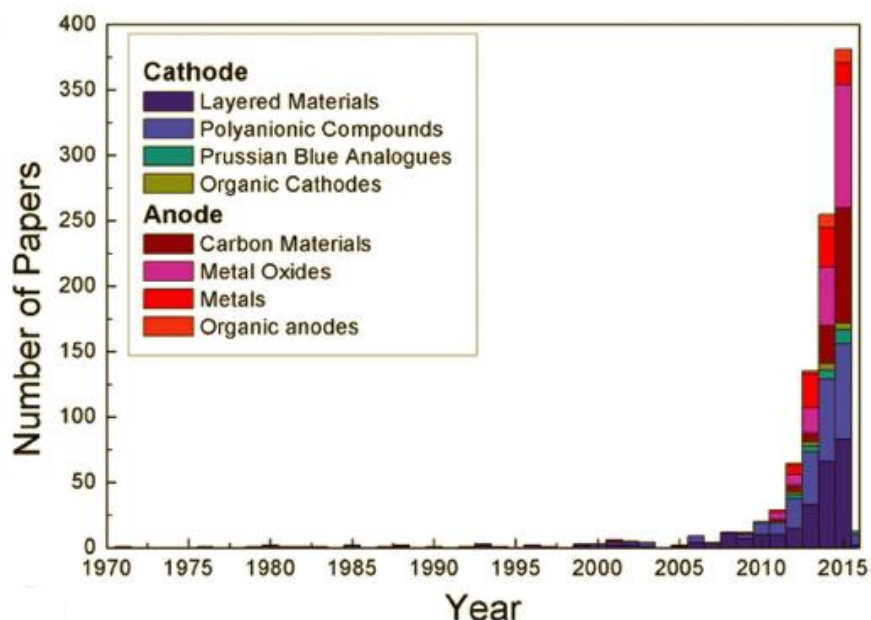
Figure 7. Number of publications, related to the sodium for energy storage devices, published in the past three decades.

The research about anodes materials in SIB's has showed three main categories (Fig. 8), based on the insertion/desertion mechanism: 1) the conversion reaction as transition metal oxides (TMO) or sulfides (TMS), where conversion reactions involve the chemical transformation of one or more of the atomic species into a host lattice to form a new compound [FFF], depending on the transition metal, insertion/desertion exhibiting a high theoretical specific capacities (*i.e.* Cu$_x$O). However, large volume expansion/contraction upon the sodiation/desodiation process accelerated tremendous damage of electrodes, which led to the loss of electrical contact and subsequently rapid capacity fading[15]; 2) the alloying reaction as intermetallic compounds, which are attractive anodes for SIBs because

they can store a large number of sodium ions in the host structure with a relatively (*i.e.* P)

at low operating potential (below 1.0 V), but suffer from huge volume expansion of the

host materials due to the continuous self-pulverization of the electrode materials[16] and; 3)

the insertion reaction as carbonaceous materials, which has the ability to accommodate

Na^+ ions into their structure[17]. In particular, hard carbon is interesting because of its

reasonable capacity of 300 mAh g^{-1} and low operating; however, the Na^+ storage

mechanism in a disordered carbon structure is still controversial[18].

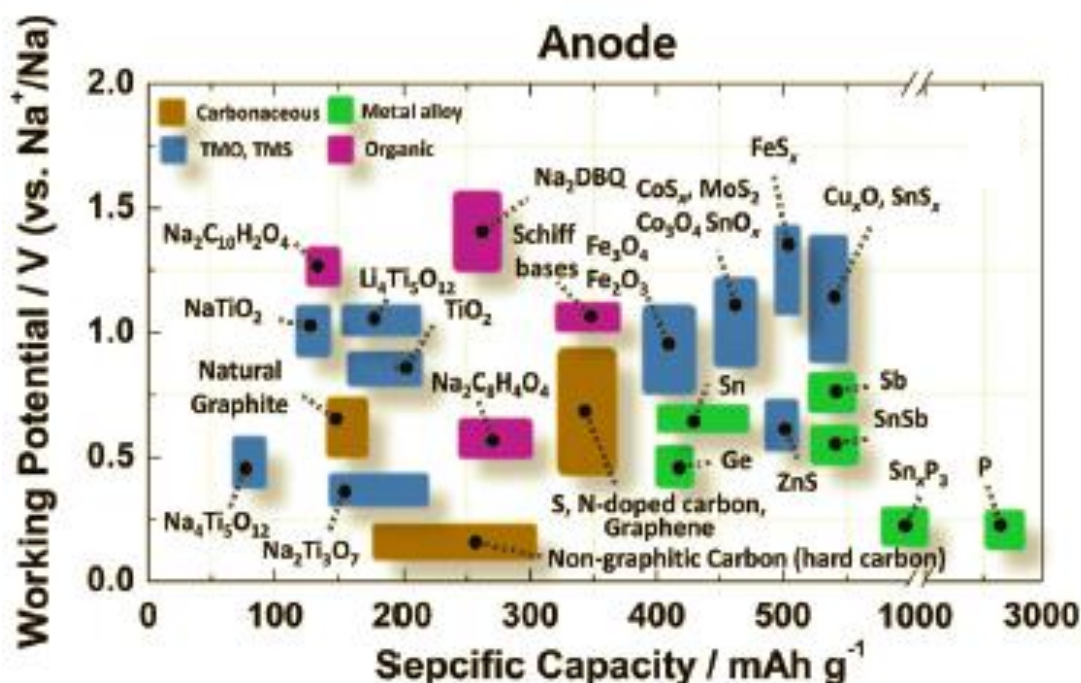Figure 7. Materials studied as Anode in SIB.

In the case of LIBs, various electrolytes, including organic electrolyte solutions, solid- and

gel-polymer electrolytes, inorganic solid electrolytes, and ionic liquids have been

investigated, and their development is still in progress. Organic electrolyte solution based

on carbonate-ester polar solvents, where sodium salts are dissolved with complex

containing functional additives, are mainly used in the practical development of SIBs due to their large potential window, high ionic conductivity and good temperature performance, however, the high risk of safety incidents in NIBs is attributed to the flammability of the organic electrolyte and the thermal runaway caused by the reactivity of the electrode materials with electrolytes. In addition, up to date, the cost of NIBs is relatively high due to the special cell assembly technology, the requirement of a strictly dry environment during manufacturing processes, and the high price of transition metals, organic electrolytes, and lithium salts. Furthermore, the limited ion conductivities of the organic electrolytes require battery designs with thin electrodes for high power and energy efficiency. As can be observed in Figure 8, the most used electrolyte has been Policarbonate (PC), however due to high free solvation energy, which induces a high-energy loss during the desolvation process (insertion), provoke a decrease in specific capacity during discharge process. So that the mixture with other organic solvents as Ethilcarbonate (EC), Dimethylcarbonate (DMC), etc. is currently under study.[4]

On the other hand, a water-based electrolyte has also been proposed as a cost-effective energy storage system, which was successfully commercialized, because: (i) the safety issue of flammable organic electrolytes is fundamentally resolved, (ii) the rigorous manufacturing conditions are avoided, and the prices of the electrolyte solvent and salts are relatively low, and (iii) the ionic conductivity of the aqueous electrolyte is higher than those of organic electrolytes by 2 orders of magnitude resulting in high round-trip efficiency and energy density even with bulky and scalable electrodes.

However, electrode materials for this system should satisfy several conditions for use in aqueous electrolytes. First, the electrode redox potentials should be located between those of oxygen and hydrogen evolution to avoid water splitting during electrochemical cycling. The potential range is dependent on the pH of the electrolyte.

Second, the electrode needs to be chemically stable at the operating pH of the aqueous electrolyte. Dissolution of materials and side reactions in the presence of O_2 should not occur. As in ARLB systems, residual O_2 can cause side reactions.

Na (intercalated) + ½ H_2O + ¼ $O_2 \rightarrow Na^+ + OH^-$ ……………………………………………………………(1)
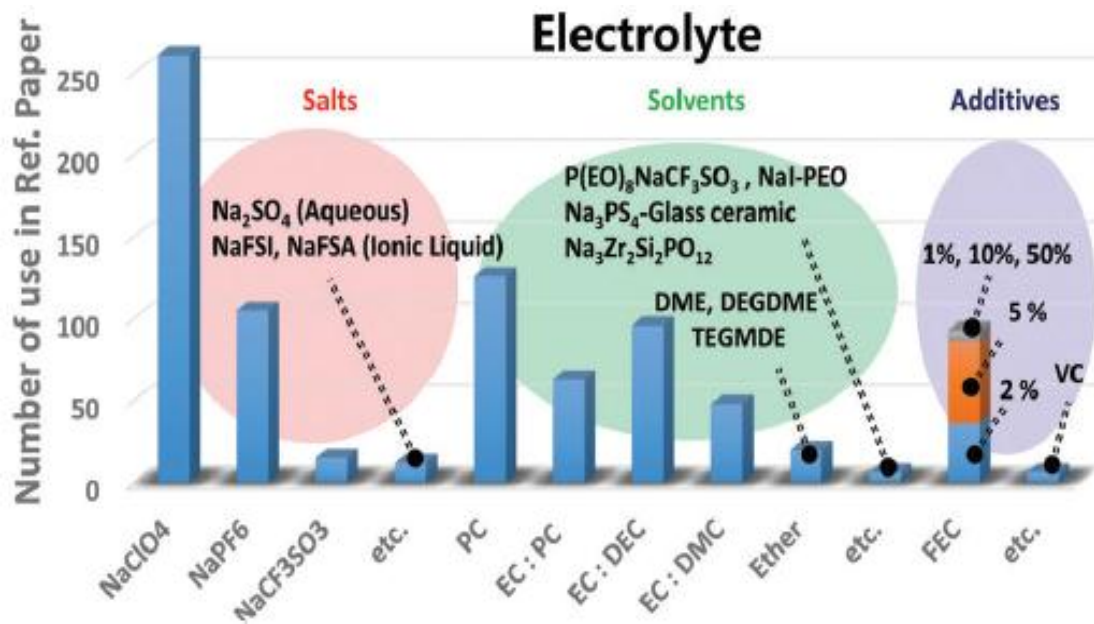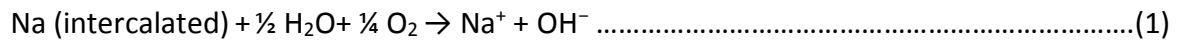

Figure 8. Electrolyte studied in SIB.

Currently have been reported different types of materials for cathode in SIB; these materials are based in sodium intercalation and exhibited a minimal structural change with intercalation, which ensures a reversible intercalation reaction that affects the cycle

life. These electrode materials are mainly categorized into: Oxides, Polyanion including Phosphates, Pyrophosphates and Fluorophosphates, Organics and Hexacyanometallates[10].

The metal oxides has a defined crystalline structure of layered compounds. These materials contain sheets of edge sharing MO_6 octahedral layers sandwiched between Na ion layers into which ionic species are inserted in an octahedral (*O*) or a prismatic (*P*) environment[19]. The number (*O2*, *O3*, *P2*, and *P3*) indicates the packing number of Na ion octahedral or prismatic layers within each unit cell. In addition, the prime symbol (*O*) indicates monoclinic distortion, such that *O'3* and *P'3* represent monoclinic distortion of the *O3* and *P3* phases, respectively, has been reported that this compounds exhibited a voltage (vs Na^+/Na) around of 3.0 V with a maximum specific capacity near to 210 mAh g^{-1} (Fig. 9). In particular, the system $Na_{0.85}Li_{0.17}Ni_{0.21}Mn_{0.64}O_2$ appears as a representative example, which shown the best results, with 3.4 V, 100 mAh g^{-1} and 98% of capacity retention at 50 cycles[20].

In comparison with oxide, transition metal polyanion materials have shown significant thermal stability, which is supported by the presence of covalent bonds such as P and O, in particular cathodes are in a deeply-charged state, however, exhibited a lower conductivity relative to oxides[21]. This system consists in corner-sharing of slightly distorted octahedral MO_6, which is linked with the tetrahedral PO_4 edge[22]. A one-dimensional Na^+ diffusion channel is clearly seen along the *b*-axis in the crystal structure, in general this material shows a maximum specific capacity closed to 150 mAh g^{-1} (Fig. 9); especially $NaFePO_4$ presented a good stability[23] 300 cycles with 94.9% of capacity retention with 152 .1 mAh g^{-1}.

The incorporation of Flour in the structure increase the operating voltage of the electrode by the high electronegativity as has been reported for Na_2CoPO_4F obtained 4.3 V[24], but with only 100 mAh g^{-1} and poor stability (85% capacity retention in 5 cycles).

Whereas organic molecules can undergo a reversible electrochemical redox reaction, the advantages of such a reaction are structural diversity, flexibility, molecular level controllability, and resource renewability. Currently, available organic cathode materials for SIBs mainly consist of aromatic carbonyl derivatives, and polymers. Several representative organic cathode materials with high specific capacities or high average operating potentials are presented in Figure 9. However, its limited use is due to low electron conductivity and high material dissolution.

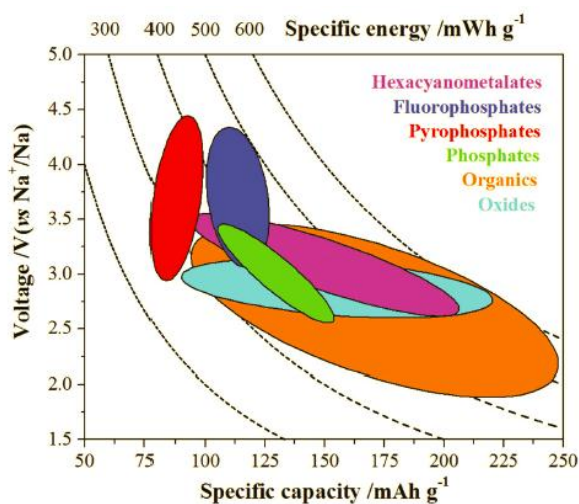Figure 9. Statistic distribution of specific capacities, operating voltage and specific energies of various cathode materials.

In general, the O-2p orbitals that σ bond to the Na impedes its motion, which can occur in the materials before mentioned. So the replacement of O^{2-} ions by $(C≡N)^{-}$ ions weakens bonding to the Na; the activation energy for Na transfer is, therefore, strongly reduced,

which makes attractive exploration of hexacyanometallates, in particular the Prussian blue analogues (PBA) or hexacyanoferrates (HCF) as cathode hosts for SIB[25].

Prussian blue analogues have large cages (*A* sites) that can accommodate various large cations. These materials crystallize in an open framework of general formula $A_xP[R(CN)_6]$ (0≤ x ≤ 2) in which P^{m+} and R^{n+} coordinate to the nitrogen and carbon ends of the CN-group, respectively, while *A* sites some atoms can be intercalated in the interstitial sites that result from the large cages, which contains zeolitic water also[26] (see Fig. 10).
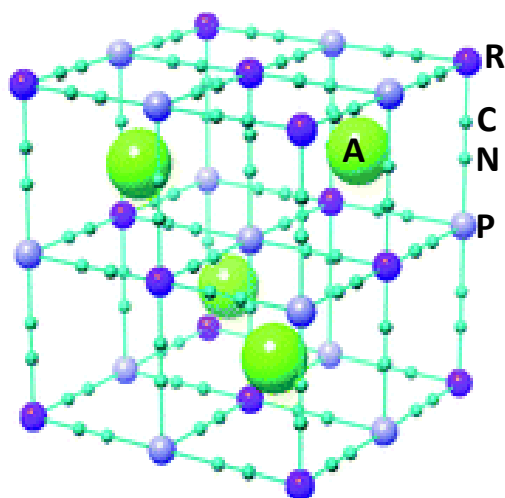
Figure 10. Prussian Blue crystal structure.

In these materials, the cyanide ligand has symmetry in their molecular orbitals, so that the energy diagram for the interaction of cation via C atom (inner metal, P) or with N end (outer metal, R) is similar; but the strength interaction in inner metal is greater that outer cation, inducing that electronic configuration in outer metal correspond to high spin. The σ interaction between atomic orbitals of the CN group and cation forming the low energy levels A_{1u}, E_g and T_{1u}, which exhibited the CN character, this interaction is affected by the polarization of N atomic orbitals towards the cation; whereas the T_{2g} *d*-orbitals in cation

interacts with π and π^* orbitals in CN ligands, inducing a transfer electronic charge from the cation to the π^* empty orbitals. This interaction promotes the electron transfer between inner and outer cation trough cyanide ligand[25].

Due to these characteristics, the Prussian blue analogues have been studied in different areas. For example, in magnetism where the magnetic interaction takes place by superexchange and spin delocalization[27]; whereas, the presences of $[P(CN)]^{n-}$ promotes that outer metal (R), which remains coordinated to water molecules for complete their coordination sphere, what promotes the protonic conductivity together with the presence of zeolitic water[28]. The water molecules removal by heating produce open metal site which can be used as catalytic sites for oxidation reaction[29] and induce the free pores with the ability to adsorb H_2 and CO_2[30].

On the other hand, the presence of 3d transition metal can be electroactive site especially in hexacyanoferrates. For this reason, this system can be applied in energy storage as capacitors and batteries mainly in SIB where sodium intercalation takes place at same time to redox process. In this context, there are some reports in the literature about the use of hexacyanoferrate as cathode for SIB in both, aqueous and non-aqueous media[31]. Previous studies on Prussian blue analogues found that thin-film NiHCF is electrochemically active in various aqueous electrolytes[32]. Moreover, a reversible redox reaction with Na at ~0.3 V (vs SCE) was confirmed to follow the reaction.

$$ANi[Fe^{III}(CN)_6] + A^+ + e^- \rightleftarrows A_2Ni[Fe^{II}(CN)_6] \quad (A = Na \text{ or } K) \ldots\ldots\ldots\ldots\ldots\ldots\ldots\ldots\ldots\ldots\ldots\ldots(2)$$
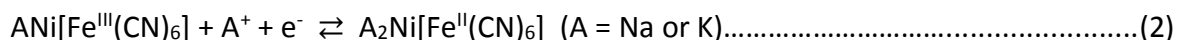
On the basis of these studies, Wessells et al. synthesized NiHCF at the bulk scale by using spontaneous precipitation in an aqueous solution. The formula of the synthesized NiCHF

was described as $K_{0.6}Ni_{1.2}[Fe(CN)_6]\cdot3.6\ H_2O$ with a theoretical capacity of approximately 85 mAh g^{-1}, however, the NiHCF electrode in 1 M $NaNO_3$ electrolyte delivered approximately 60 mAh g^{-1} at 0.83C with a redox potential of 0.59 V vs SHE. High rate capability was obtained up to 41.7 C with a cycle life of over 5000 cycles at 8.3 C[33]. They also confirmed that approximately 0.18% of the isotropic lattice strain was applied in NiHCF during the charge/discharge reaction[34].

Although promising electrochemical behavior has been observed in NiHCF, the redox potential of 0.59 V vs SHE is relatively low for it to be used as a cathode. To address this, Wessells et al. performed a similar study on CuHCF, which exhibited higher redox potential vs SHE. The chemical formula of CuHCF was $K_{0.71}Cu[Fe(CN)_6]_{0.72}\cdot3.7H_2O$. They found that CuHCF operated at a redox potential of approximately 1.0 V vs SHE with a specific capacity of $\sim$60 mA h g^{-1}. Relatively good rate performance of up to 41.7 C was obtained, retaining $\sim$34% of the low rate capacity[35]. Capacity retention of approximately 77% was observed after 500 cycles at 8.3 C. Interestingly, Na^+ and Li^+ cycling in CuHCF exhibited generally faster cycle degradation than that of K^+ and NH_4^+. Recently, Wessells et al. reported solid-solution phases of CuNiHCF synthesized using a previously described coprecipitation method[36]. They found that redox potentials can be tuned from 0.6 to 1.0 V using a $Cu_xNi_{1-x}HCF$ electrode in a 1M $NaNO_3$ aqueous electrolyte. The redox potential increased from 0.6 to $\sim$1.0 V as the Cu content increased without significant capacity loss. Stable cycle performance of up to 2000 cycles was also achieved for the solid-solution phase of $Cu_{0.56}Ni_{0.44}HCF$; after Hung et .al. reported that this improvement is associated to tunable potential phenomena[37].

On the other hand, while the series of Ni- and Cu-based Prussian blue cathodes exhibited high rate capability and stable cyclability, these compounds cannot be paired with conventional Na-free anodes because they initially exist in a charged state. Therefore, Wu et. al. introduced sodiated Prussian blue analogues of Na_2CuHCF as cathodes presents the charge/discharge profiles of the Na_2CuHCF electrode vs a Ag/AgCl reference electrode at a current density of 65 mA g^{-1} in a 1 M Na_2SO_4 electrolyte (pH 7). With sodiated Prussian blue, a reversible capacity of 65 mA h g^{-1} was still obtainable at a redox potential of 0.4–0.6 V, shows that the electrode could sustain a capacity of ~61 mA hg^{-1} at 10 C. Stable cycle performance of up to 500 cycles at 5 C was observed for Na_2CuHCF[38]. Whereas, Wu et. al. reported a vacancy free $Na_2Co[Fe(CN)_6]$ nanocubes synthesized by a controlled crystallization reaction and reveal its reversible Na-storage behavior as a new aqueous cathode. Due to its perfect lattice framework with two redox-active sites, this material exhibits a high reversible capacity of 130 mAh g^{-1}, a strong rate capability at 20 C rate and a superior stability with 90% capacity retention over 800 cycles[39]. On other hand, synthesized low-defect Prussian blue $Fe[Fe(CN)_6]$ nanocrystals and revealed their Na-storage performance in aqueous electrolytes. Benefitting from its suppressed lattice defects and well defined nanocubic morphology, the as-prepared Prussian blue nanocrystals exhibit a greatly improved capacity of ~125 mAh g^{-1}, a strong rate capability with 102 mAh g^{-1} at a high rate of 20C and a remarkably long cycle life with 83% capacity retention over 500 cycles[40]. Recently, has been reported that Vanadium Hexacyanoferrate provide a high recycling efficiency with a specific capacity of 90 mAh g^{-1}, taking advantage of the multiple-electron redox reactions of V and Fe ions[41].

On the other hand, since Goodenough reported in 2012 the use of Hexacyanoferrates $K_xM[Fe^{III}(CN)_6]\cdot H_2O$ (M: Co, Fe, Ni, Mn, Cu and Zn) as cathode for SIB, the interest in this open framework materials for batteries increased, due to that are easily synthesized and have a low cost[25]. With the aim to enhance the electrochemical behavior different strategies are proposed.

a) The use of sodium ferrocyanide ($[Na_4Fe(CN)_6]$) as molecular block in the structure increases the amount of sodium in the synthesized material; when the outer metal is Co^{2+} or Mn^{2+} increases the specific capacity[42].

b) The mixture of two different cations in the outer sphere, e. g. $Na_{1.76}Ni_{0.12}Mn_{0.88}[Fe(CN)_6]_{0.98}\cdot H_2O$, $Na_{0.39}Fe_{0.77}Ni_{0.23}[Fe(CN)_6]_{0.79}\cdot 3.45H_2O$ and $Na_2Ni_{0.4}Co_{0.6}Fe(CN)_6$, favors a better stability during charge/discharge process[43].

c) The synthesis of core-shell of hexacyanoferrates (Figure 11) as Fe-HCF@Ni-HCF, increases the electrochemical stability, whereas, Cu-PBA@Ni-PBA, improves the capacity retention at different C-rates[44].
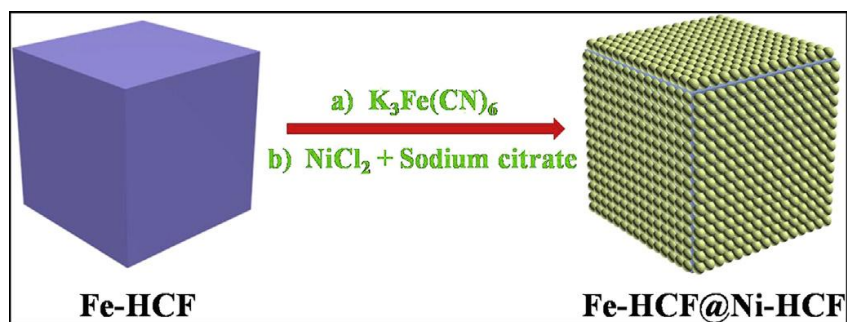
Figure 11. Schematic representation of synthesis procedure of Fe-HCF@Ni-HCF composite

d) The synthesis of materials with low defects due to presence of vacancies by the absence of $[Fe(CN)_6]^{n-}$ (Figure 12), increases the specific capacity due to the high amount of sodium in the structure[45].
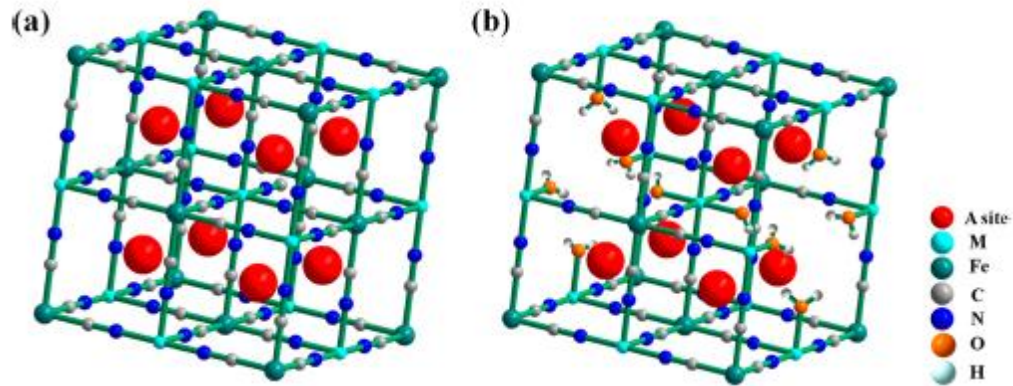
Figure 12. Schematic crystal structure of Hexacyanoferrates a) without and with ferrocyanide vacancies.

e) The water removal in the framework, which induces structural changes, increases the sodium-framework interaction improving the electrochemical performance as was reported by Song et. al. (Figure 13)[46].
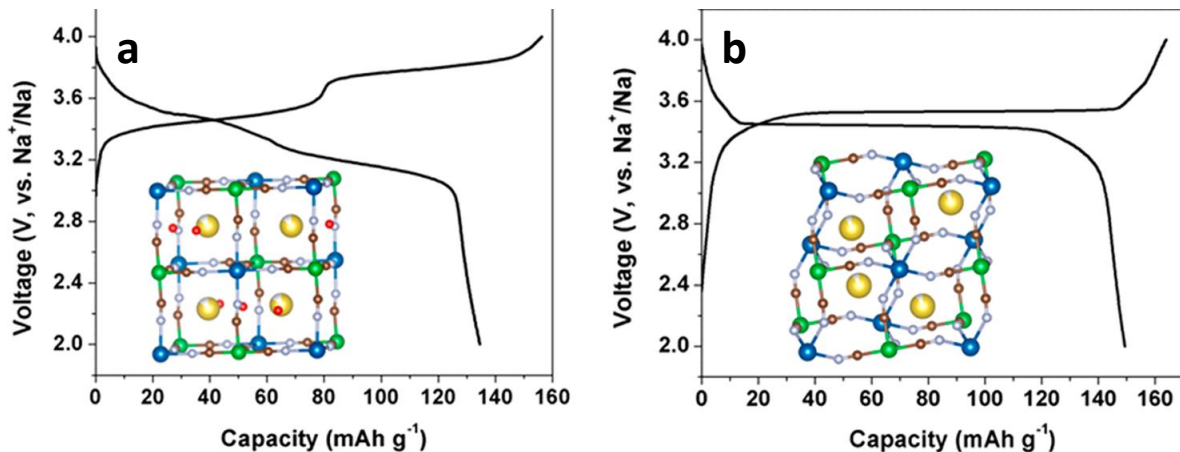
Figure 13. Charge/discharge profile at 0.1C in a) Hexacyanoferrate of Manganese with zeolitic water in monoclinic cell and b) same material without water in rhombohedral cell.

In this context, the present thesis relates the crystalline structure and its physico-chemical properties with its electrochemical performance as cathode in aqueous and non-aqueous batteries. In aqueous media, the effect of second compensating cation in the stability of $Na_2Zn_3[Fe(CN)_6]_2$ during charge/discharge process is reported, whereas for $Na_{2y}Co_{1-x}Mn_x[Fe(CN)_6]_y$ the interaction between outer metal and their effect over structural stability during sodium insertion/desertion was considered.

On the other hand, in non-aqueous media the effect of water inside the structure in $Na_2Zn_3[Fe(CN)_6]_2$ over the sodium diffusion and therefore in their electrochemical behavior were studied. Furthermore, the effect of a dopant outer cation in $Na_{2y}M_{1-x}Mn_x[Fe(CN)_6]_y$ (M: Co, Ni and Fe) over the Jahn Teller distortion exhibits by Mn^{3+} during redox process is studied.

CHAPTER 2.

2. Experimental Section

2.1 Synthesis of materials to be studied

The Na^+ and K^+ containing materials, $Na_2Zn_3[Fe(CN)_6]_2 \cdot xH_2O$ and $K_2Zn_3[Fe(CN)_6]_2 \cdot xH_2O$, were prepared by the precipitation method mixing aqueous solutions of $Zn(NO_3)_2$ and $Na_4[Fe(CN)_6] \cdot 10H_2O$ (or $K_4[Fe(CN)_6] \cdot 3H_2O$) at 60°C under stirring and then aging the formed precipitates within the mother liqueur for a week at room temperature.

The formed solid was then separated from the liquid fraction by centrifugation, washed several times with distilled water to remove all the accompanied ionic species, and finally dried at room temperature until it had constant weight. The Rb and Cs containing solids were obtained by ionic exchange from $K_2Zn_3[Fe(CN)_6]_2 \cdot xH_2O$ using a known preparative route [32], the materials were labeled NaZnHCF, KZnHCF, RbZnHCF and CsZnHCF.

The dehydrated structure was obtained from heat treatment at 230 °C in vacumm of $Na_2Zn_3[Fe(CN)_6]_2$ for 12 h, the material was labeled D-NaZnHCF.

On the other hand, The $Na_{2y}M_xMn_{1-x}[Fe(CN)_6]_y$ was obtained by co-precipitation method; from the mixture of solution A (0.1 M of $Na_4Fe(CN)_6$) and solution B (0.1 M of Sodium Citrate and 0.05 M of $Mn(NO_3)_2$ and 0.05M of $M(NO_3)_2$, where M= Ni and Co; except for iron where the salt use is $FeCl_2$) in the Y-type micro-mixer, using a peristaltic pump at 20 rpm, The solution was stirred for 12h at room temperature, and then the resulting

precipitate was washed with water and ethanol several times, and finally dried under vacuum at 50 °C for 24 h.

2.2 Electrode preparation

Slurries containing the as-synthesized hexacyanoferrates, amorphous carbon (Timcal SuperP Li), polyvinylidenedifluoride (aldrich), and graphite natural (Alfaesar) in a ratio of 80:9:9:2 were prepared in Tetrahydrofuran. These slurries were deposited on carbon plate (Fuel Cell Grade) for aqueous media whereas for non-aqueous media the slurries was deposited over Al foil, the electrode was dried at 60 °C under vacuum for 12 hr.

2.3 X-Ray Diffraction

The materials elemental composition was determined by optical emission spectrometry using inductively coupled plasma (OES-ICP), with a Perkin Elmer OPTIMA 8300 spectrophotometer. X-ray powder diffraction (XRD) patterns were collected with a D8 Advance diffractometer (from Bruker) in the Bragg-Brentano configuration using CuKα radiation (λα = 1.5418 Å).

2.4 Vibrational Spectroscopy

The IR spectra were collected by ATR using a spectrophotometer Spectrum One from Perkin Elmer; the Raman spectrum were obtained in using a DXR spectrometer (from Thermo Scientific) with a laser 532 nm. The in situ infrared were recorded with an FTIR Perkin Elmer spectrometer using a SP-02 spectroelectrochemical cell from Spectroelectrochemistry Partners, the cell was coupled on a Pike MIRacle ATR system.

2.5 Electronic Spectroscopy

Electron paramagnetic resonance (EPR) spectra of powder samples were recorder using a Bruker Elexsys E580 EPR spectrometer operating at X-band frequency (9.4186 GHz) equipped with 100 kHz field modulation and phase sensitive detection to obtain the first derivative signal.

2.6 Mossbauer Spectroscopy

^{57}Fe Mössbauer spectra were recorded using a constant acceleration spectrometer from Austin Scientific Associates and 57Co/Rh source. An iron foil was used as reference material for the Mossbauer isomer shift and for the velocity scale calibration.

2.7 Electrochemical Measurement

For aqueous media, three electrode cell containing ZnHCF working electrode, an Ag/AgCl reference electrode and large partiatelly charge ZnHCF as counter electrode. Electrochemical analyses were carried out at room temperature in a potentiostat–galvanostat PGstat302N, whereas for non-aqueous media an electrochemical performance were evaluated in a battery test cell from bio-logic, and is composed of a cathode and a metallic-sodium anode with 1 mol L^{-1} NaPF$_6$ in 1:1 dimethyl carbonate/ethylene carbonate electrolyte, a Whatman glass-fiber separator. The electrochemical data were recorded with a potentiostat–galvanostat SP300 (from Bio-logic)

CHAPTER 3.

3 Results and Discussion (Zinc Hexacyanoferrate)

3.1 Aqueous Media

The tridimensional (3D) crystal structure for the series $Zn_3A_2[Fe(CN)_6]_2 \cdot xH_2O$ with A = Na, K, Rb, Cs, is formed by the assembling of FeC_6 octahedra and ZnN_4 tetrahedra, resulting a porous framework with ellipsoidal cavities of about 15.5 x 11.1 x 7.9 Å, which remain communicated by elliptical windows of *c. a.* 6.8 x 8 Å[47]. Such large windows size makes possible the mobility of the charge-balance alkali ion in the solid and, in fact, these solids are usually prepared by ionic exchange from a single composition, ZnHCF in SIB´s was first reported by Lee et. al., showing a reversible capacity of 56.4 mAh g^{-1} at 0.18 C and good stability for 50 cycles with capacity retention of 95%, no phase changes during Charge process is found[48]. The electrolyte used was EC/DMC because this solvent mixture has similar physical properties as dielectric constant, viscosity, and electric dipole moment to those of water; thus, aqueous electrolytes are expected to improve the cycle life significantly. However, studies in aqueous media have shown instability of ZnHCF during insertion / desertion of the sodium ion due to those electrochemical redox reactions will induce frequent rhombic–cubic phase transitions and successive acceleration of ZnHCF dissolution[49].

In this context, the ZnHCF synthesized according to description in Chapter 2 was evaluated as cathode in aqueous media modifying the compensation cation within the structure.

3.1.1 Structural Characterization.

The powder XRD patterns for every material were refined by Le Bail method showed that these materials crystallize with a rhombohedral unit cell in the *R-3c* space group (Fig. 14) without any impurities.
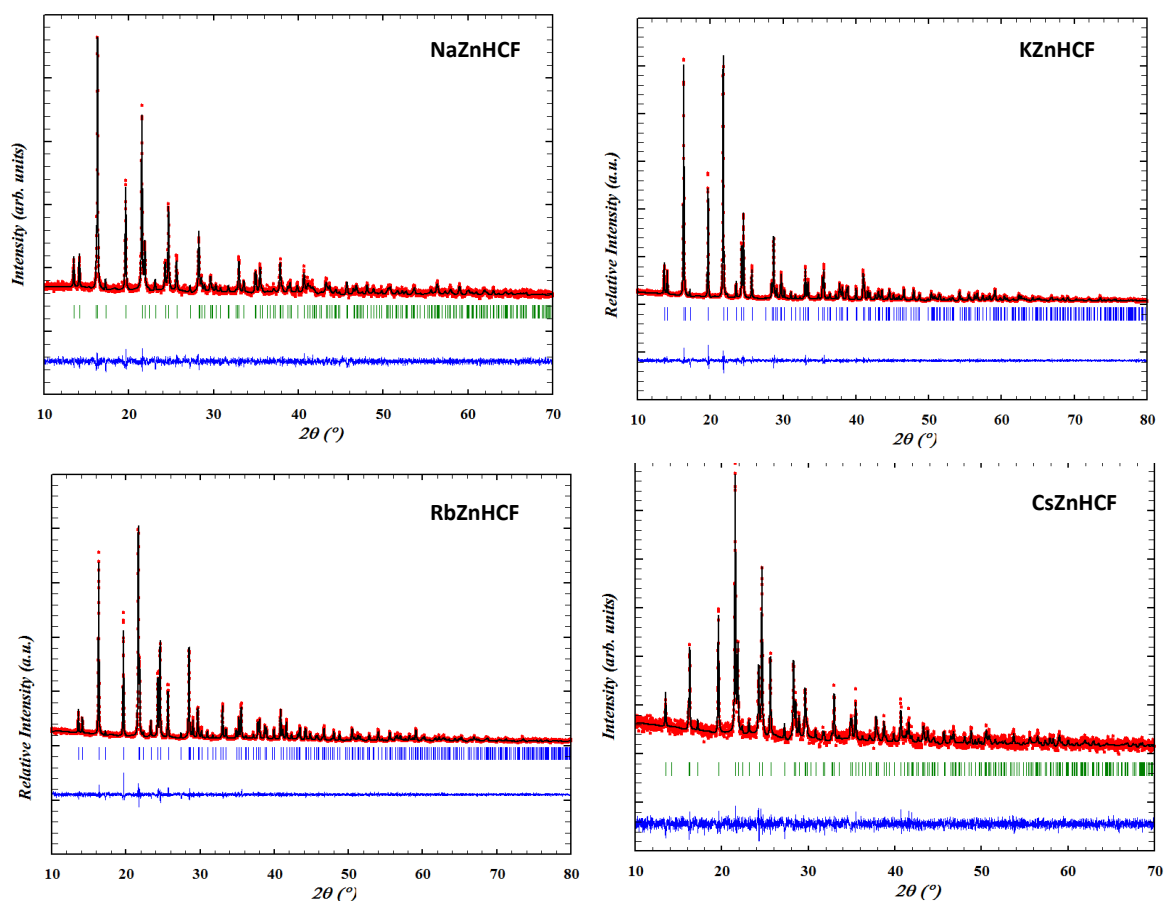

Figure 14. Powder X-ray Diffraction, with a Le Bail profile fitting for the materials under study.

To understand the results to be discussed below, the availability of a picture of the porous framework of these materials is convenient. Figure 15 shows such figure prepared using Diamond software for structure drawing using the reported CIF files for the materials under study. As already mentioned, such framework can be considered as resulting from the assembling of FeC_6 octahedra and ZnN_4 tetrahedra in a 2:3 ratio. In transition metal cyanometallates, the coordination at the C end is characterized by a strong π-back bonding interaction. The charge removed from the inner metal, in this case Fe, through that mechanism is located at N end, related to a higher electronegativity for the N atom compared with C one. Such charge concentration effect on the N atom modulates its basicity and interaction with transition metal ions (Lewis acidic species). The tetrahedral coordination to the Zn atom, with a $\angle$CN-Zn-NC angle of 108 $^{\circ}$, is unfavorable for a pronounced charge donation to the metal (Zn) because the coordination bond formation takes place through the 5σ orbital of the CN group. From this fact, a large fraction of the charge removed from the iron atom, through the π-back bonding mechanism, remains located at the N atom and determine the framework electrostatic interaction with the exchangeable metal (A). The exchangeable metals are found close to the framework N atoms. The high frequency impedance spectra for the iron series suggest that a small cation, like Na^+, with a high polarizing power, occupies a structural position close to the N atom, but for a bulky cation, e.g. Cs^+, it is found at an intermediate position between two neighboring N atoms[50]. The N-N distance is 3.2 Å, within a same tetrahedron, and 4.3 Å between N toms from neighboring tetrahedra. The cation size (diameter), in Å, is: Na: 1.98, K: 2.74, Rb: 3.04, and Cs: 3.34. A comparison between the N − N distance and the

cation diameter, suggests that large cations, e.g. Rb, Cs, as naked species, are probably found interacting with two neighboring N atoms from a same tetrahedron. This favors a stronger cation electrostatic interaction with the framework surface. A given cavity contains two exchangeable cations, located at the largest possible distance between them in order to minimize the repulsive interactions. The free spaces (cavities) for the materials under study have enough volume to accommodate the alkali metal ion and water molecules in its environment (the solvation sphere). The available free space to accommodate these water molecules, and the solvation energy, follow the order Na > K > Rb > Cs. For a small cation, the distance to the charge center is short, and the attractive cation – water molecule electrostatic interaction is strong. The passing of cations through small windows, supposes the removal of water molecules from their solvation sphere, which involves certain energy (the desolvation energy). This process is more favorable for large cations. For the materials under study, the windows size is enough large to allow the cations diffusion as partially hydrated species[51].

The removal of the alkali ion from the porous framework supposes the oxidation of the iron (III) atom within the $[Fe(CN)_6]$ octahedral block, to form $Zn_3[Fe(CN)_6]_2$. This is a stable phase for zinc hexacyanoferrate (III), with a unit cell and framework topology similar to those reported for the series $Zn_3A_2[Fe(CN)_6]_2 \cdot xH_2O$.

This facilitates the redox reaction and mobility of the alkali metal through the porous framework. In an aqueous electrolyte and extraction of only a fraction of the alkali metal, partial redox reaction, results a mixture of ferrous and ferric building blocks, and the resulting solid would be a solid solution within a same structural network. Such solution is

a stable rhombohedral phase for zinc hexacyanoferrate (II, III). Zn hexacyanoferrate (III) can be stabilized as an hydrated phase doping the structure with a small fraction of Fe(II) species, which is accompanied by the presence of charge balance cations within the cavities[47].
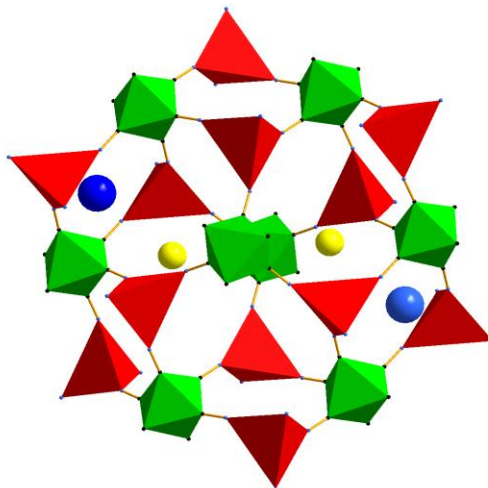
Figure 15. Porous framework for the series $Zn_3A_2[Fe^{II}(CN)_6]_2$. A given cavity accommodates two A^+ cations. The framework negative charge is accumulated on the N atom (the tetrahedron corners). A small cation, like Na^+ (yellow sphere), is probable found close the N atom, but a large one, like Cs^+ (blue sphere) probably occupies an intermediate position between two neighboring corners.

3.1.2 Cyclic Voltammetry.

Figure 16 shows the cyclic voltammetry curves, recorded in ANO_3 aqueous solution (1 mol.L^{-1}) at 1 mV.s^{-1} for the series of ionic conductors under study. The redox processes observed in the i-E curves correspond to Fe^{3+}/Fe^{2+} redox couple in the octahedral $[Fe(CN)_6]^{n-}$ building unit, according to Eq. (1):

$$Zn_3A_2[Fe^{II}(CN)_6]_2 \cdot xH_2O \rightleftarrows yA^+ + Zn_3A_{2-y}\{[Fe^{II}(CN)_6]_{2-y} [Fe^{III}(CN)_6]_y\} \cdot xH_2O + ye^- \ldots\ldots\ldots\ldots(3)$$

This charge balance equation corresponds to a reversible redox process and to the cation A^+ migration from the cavities system of the porous solid to the solution and vice versa. It can be observed that both, the anodic and cathodic peaks, are broad and asymmetrical signals, which was ascribed to the availability of many sites for the cation within the cavity. During the extraction process the cation probably jumps between different sites (potential wells) within the cavity before its migration to the electrolyte. Such jumping process within the cavity delays its extraction from the solid and broads the signal. Certain dependence of this effect on the amount of exchangeable metal within the cavity is expected. The smaller peak width was observed for K, which was interpreted as resulting from a lesser effective cation size considering the solvation sphere. Rb^+ and Cs^+ are less polarizing cations, with a thinner solvation sphere but with a larger size and weight. From the recorded voltammetry curves, the anodic and cationic exchanged charge, Q_a ($C.g^{-1}$) and Q_c ($C.g^{-1}$), respectively, and the redox peaks separation (ΔE_p), were calculated.

These parameters show a definite decreasing correlation with the cation weight (see Inset of Figure 16 and Table 2). For faradic charge (Q) such behavior was ascribed to a kinetic effect related to a lower mobility for bulky and heavy cations. The removal of a heavy cation requires of a higher voltage and thus the storage energy density is larger, but such favorable possibility is affected by the cation lower mobility through the porous framework. The value of ΔE_p shows a decreasing behavior on the cation size. This peak separation is an important factor for energy loss in a battery. A small ΔE_p value means low polarization overpotential (good reversibility and fast kinetic reaction). As already

mentioned, a bulky cation, due to its low polarizing power and related low solvation energy, is more easily transfer from the electrolyte to the material porous framework, but with a low mobility.
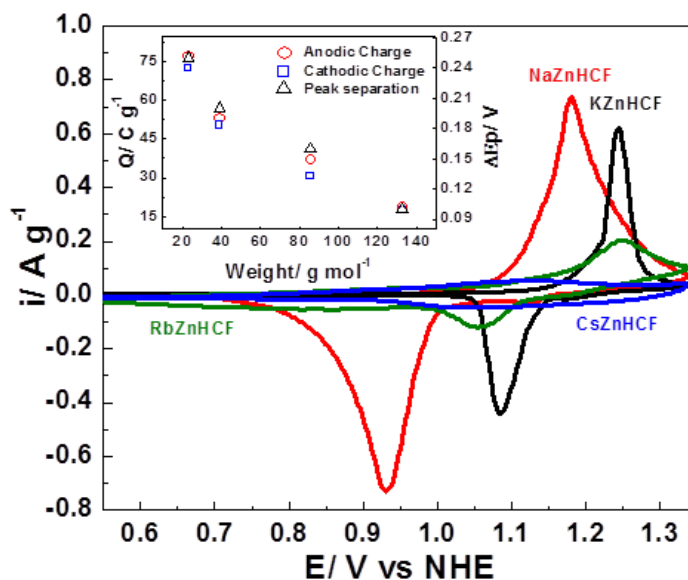
Figure 16. Cyclic Voltammetry after 6 cycles of NaZnHCF, KZnHCF, RbZnHCF and CsZnHCF in ANO$_3$ (1 mol L^{-1}) where A: Na (red line), K (black line), Rb (green line) and Cs (blue line) at 1 mV s^{-1} . Inset: anodic/catodic charge and peak separation vs cation weight.

The order found for the formal potential (E$_f$) is Na$^+$ < K$^+$ > Rb$^+$ > Cs$^+$ (Table 2). The values for E$_f$ parameter were calculated according to E$_f$ = (E$_{p,a}$ + E$_{p,c}$)/2 where E$_{p,a}$ and E$_{p,c}$ are the positions for the anodic and cathodic peaks, respectively. For cubic transition metal (M) hexacyanometallates (Prussian blue analogues), positive correlations for the E$_f$ values with the polarizing power for the metal (M) linked to N end of the CN ligand have been observed[52]. The polarizing power senses the metal capability to subtract electron density from its ligands. As already mentioned, the charge balance cation (A$^+$) is located close to the N atoms at the cavity surface, polarizing their charge density, which results in an

increase for the charge subtraction from the iron (II) via π-back bonding. For Na^+, related to its small size, the water molecules in the solvation sphere remain firmly tied, partially shielding its charge subtraction capability from the N atoms. This explains the smallest E_f value found the solid containing Na^+. The order observed for the remaining metals (K^+ > Rb^+ > Cs^+) is consistent with their size and polarizing power as naked species; Cs^+ is the soft cation within the series.

Table 2. Summary of results from cyclic voltammetry curves for the materials under study

Compound	E_f, in V/NHE	ΔE_p, in V	Q_a, in C g^{-1}	Q_c, in C g^{-1}
NaZnHCF	1.055	0.25	79	74
KZnHCF	1.160	0.20	54	50
RbZnHCF	1.150	0.16	35	30
CsZnHCF	1.070	0.10	20	19

3.1.3 Effect of the presence of a second cation.

Transition metal hexacyanoferrates exhibit cation exchange properties. Under thermodynamics equilibrium, the order in which the alkali metals can displace one another is: Cs > Rb > K > Na[51], thus these materials have been used for cesium removal from liquid radioactive wastes; particularly, transition metal hexacyanoferrates (II) exhibit high sorption properties for cesium(+) since they have a high affinity towards this ion. The stability of the structure containing Cs^+ is related to the size of this metal and possibility to interact with two N ends at the same time.

Figure 17 shows the i-E characteristic curves for KZnHCF and RbZnHCF after 6 cycles at 1 mV s^{-1} in NaNO$_3$ (1M). No appreciable changes are observed in these curves under such conditions.
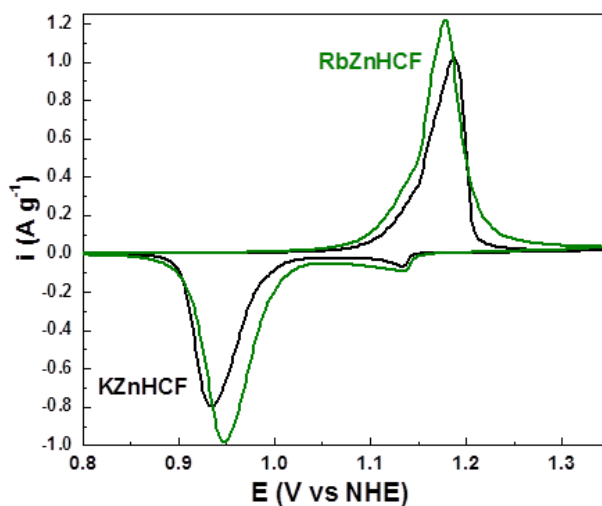
Figure 17. Cyclic Voltammetry after 6 cycles of KZnHCF and RbZnHCF NaNO$_3$ (1 mol L^{-1}) at 1 mV s^{-1}.

The results show E$_f$ and ΔE$_p$ values close to 1.06 and 0.24 V, respectively, in both systems. These values are similar to those observed for NaZHCF (Table 1). Regarding the involved charges, for KZHCF, the values of Q$_a$ and Q$_c$ are, 74 and Q$_c$= 70 C g^{-1}, respectively, slightly smaller than the values found for RbZHCF (Q$_a$= 77 and Q$_c$= 72 C g^{-1}). This suggests that during redox process K$^+$ and Rb$^+$ are displaced by Na$^+$, because sodium exhibits a higher mobility inside the cavity. Such ionic exchange was verified by EDS analysis after samples were submitted to voltammetry characterization (see Figure 18).

Before to electrochemical experiments

After 6 CV cycles in $NaNO_3$ as electrolyte
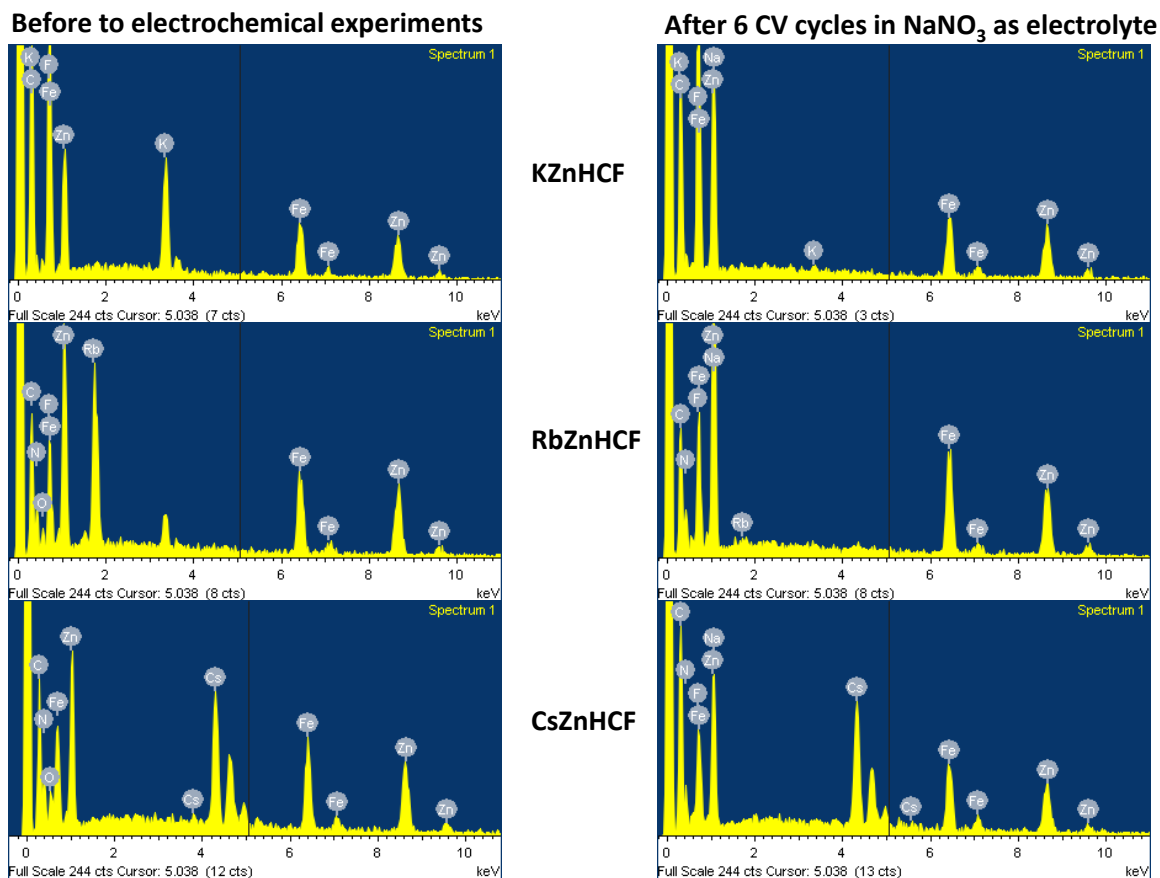
Figure 18. EDS spectra recorded before and after electrochemical process.

The electrochemical response of CsZnHCF after several cycles of voltammetry in $NaNO_3$ aqueous solution shows a behavior quite different to fresh CsZnHCF and NaZnHCF samples (see Fig. 19A). EDS spectra show (Fig. 18) that under such conditions, a mixed Cs and Na composition, in following labeled as CsNaZnHCF, is obtained. The calculated anodic and cathodic charges for this last composition are 49 and 47 $C.g^{-1}$, respectively. The formation of the mixed composition is confirmed, using an Electrochemical Quartz Crystal Microbalance (EQCM), during the Cyclic Voltammetry experiment (Figure 19b). The mass

change during the polarization sweep for CsZnHCF, in comparison with that obtained for NaZNHCF. Once the mixed composition, CsNaZnHCF is formed, the mass change corresponds to the insertion/extraction of Cs^+.
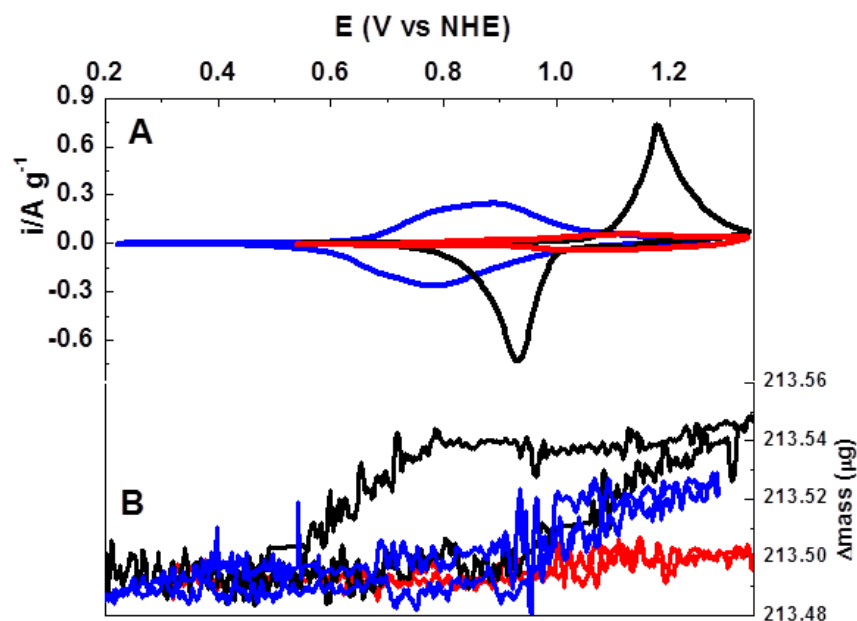
Figure 19. A) Cyclic Voltammetry and B) EQCM after 6 cycles of NaZnHCF (red line), CsZnHCF (black line) in ANO$_3$ where A: Na, and Cs (1 mol L^{-1}) and CsZnHCF in NaNO$_3$ labeled CsNaHCF (blue line) at 1 mV s^{-1}.

According to the recorded EDS spectra after 6 voltammetry cycles, the Na/Cs atomic ratio results 0.9, which corresponds to the following formula unit, $Na_{0.75}Cs_{1.25}Zn_3[Fe(CN)_6]_2$. The peak to peak separation is 0.11 V, suggesting that cation diffusion is faster for Cs^+. It seems, the dominant factor in such easy diffusion for a heavy metal like Cs, is the low polarizing power for Cs^+, and from this fact, its low solvation energy, facilitating the transport from the electrolyte to the material porous framework. The presence of both, Na^+ and Cs^+ inside the cavity probably minimizes the cation-cation repulsive interaction and the same time modulating the cation - framework electrostatic forces to favor a

reduction in the redox potential, to a value of E_f = 0.83V/NHE. Within the series of materials under study, the best electrochemical performance was observed for the mixed composition, CsNaZnHCF. From this fact, the galvanostatic and impedance studies were limited to NaZnHCF and CsNaZnHCF samples in $NaNO_3$ aqueous solution.

3.1.4 Galvanostatic experiments.

Figure 20 shows the behavior of NaZnHCF in $NaNO_3$ (1 mol L^{-1}) under charging/discharging cycles at 0.36 C, where the system is reversible (for this study, 60 mA g^{-1} is defined as 1C). For the first charging cycle, a flat plateau at the potential range 0.95-1.05 V/NHE appears. The maximum charging specific capacity is 38 mAhg^{-1}, a relatively low value compared with the theoretical capacity for NaZnHCF, which is 64.8 mAhg^{-1}.
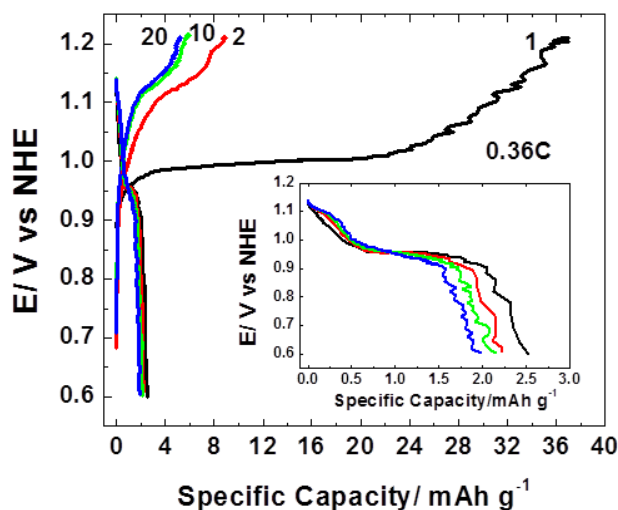

Figure 20. Galvanostatic charge/discharge profile for NaZnHCF in NaNO3 solution at 0.36 C.

The discharge process reveals that the material specific storage capacity is also very low. On the charge/discharge cycles, the solution turns yellowish, which suggests that a

fraction of the complex anion $[Fe(CN)_6]^{3-}$ partially decomposes. Zhou et al. have reported an analogue behavior for hexacyanometallate-based solids[49].

Ex-situ Raman spectra were recorded to illustrate the change in valence state for the hexacyanoferrate ion during the charge/discharge cycles. The $v(CN)$ stretching vibration is an excellent sensor for the valence of the metal involved in the hexacyanoferrate anion, with a frequency shift above 60 cm^{-1}, in the oxidation process, from Fe^{2+} to Fe^{3+}. For the materials under study, such frequency shift is close to 70 cm^{-1}, from 2080 to 2150 cm^{-1} (Figure 21A). The appearance and intensity of these two $v(CN)$ bands are sensor for the redox reaction associated to the cation release and insertion from the solid structure. According to the intensity of that band, always a mixture of the reduced and oxidized phases is obtained. Figure 21B shows the galvanostatic curves for CsNaZnHCF at 0.36C after 6 cycles of cyclic voltammetry. A plateau between 0.7-0.9 V/NHE is observed, with a specific charge capacity of 40 mAh g^{-1}, which suggests that 1.25 mol of cations are involved in the charge/discharge cycles, This value is similar to the one obtained for Cs ion from EDS spectra after electrochemical cycles (Fig. 18), indicating that on the oxidation process only Cs^+ is released from the structure. This is corroborated by the recorded EQCM data (Figure 19B). During the reduction process, the specific discharge capacity results 37 mAhg^{-1}, corresponding to the insertion of 1.15 mol of cations. The specific capacity of charge and discharge decreases with the cycle number (Figure 21B), for 40 cycles, the specific charge capacity results 27.5 mAhg^{-1}, equivalent to a charge retention of 75%. During the discharge, the specific charge capacity is 25 mAhg^{-1}, for a retention capacity of 65%, this material shows a decrease in its storage capacity of 32.5 mAh g^{-1} at

0.72 C and 28 mAh g^{-1} at 1.4 C (Fig. 21C). Such behavior can be associated to the fact that in the solid the Cs$^+$ ion can be displaced by sodium due to its excess concentration in the electrolyte, reducing iron sites involved in charge/discharge process. The specific capacity depends on the cation insertion/desertion and on the redox sites involved during charge/discharge process, which should occur at same time. From the presence of Cs in the framework, a decrease for the energy storage capacity is expected because its lower mobility, but not previous evidence in this sense is available.
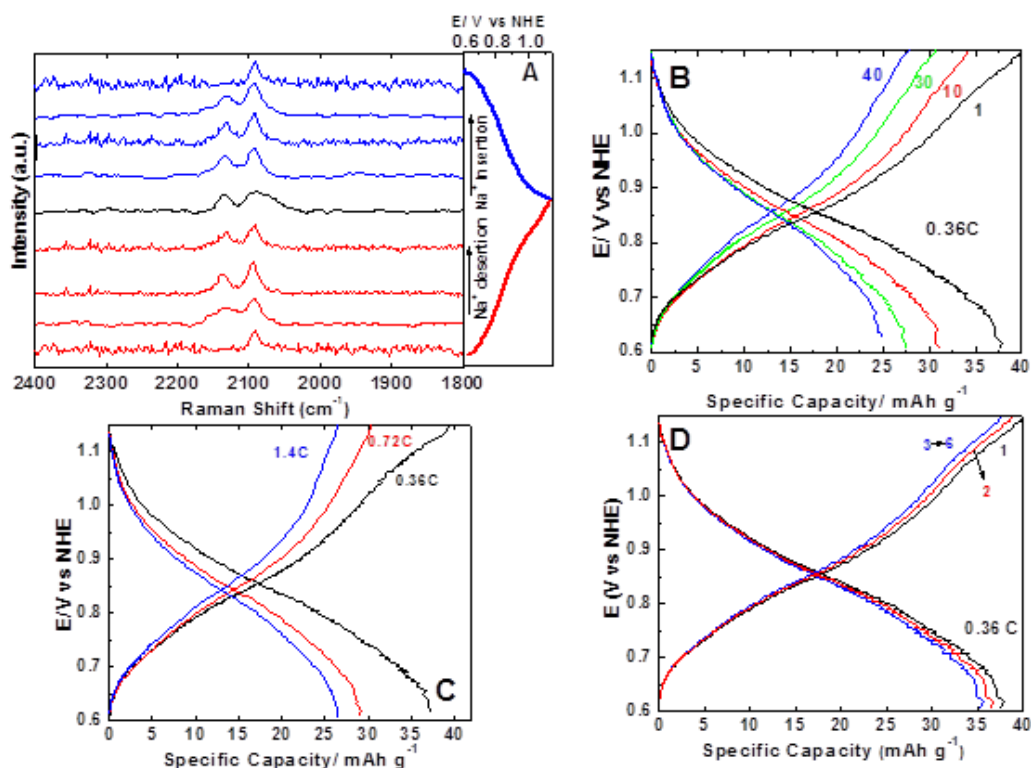
Figure 21. (A) Ex-situ Raman spectra of CsNaZnHCF at different potential, (B) The cycle life of CsNaZnHCF at 0.36 C, (C) Galvanostatic charge/discharge at different rate and (D) Galvanostatic charge/discharge at 0.36 C, after 40 cycles and 15 minutes of static conditions.

On the other hand, with the aim to verify the cation exchange capacity of hexacyanoferrate in static condition, the electrode CsNaZnHCF previously used during 40 charge/discharge at 0.36C, was immersed during ten minutes in a solution of CsNO$_3$ (0.1

M), regenerating the initial system as is observed in Figure 21D, where the specific capacity (curve 2) is similar to that observed in curve 1. This process was evaluated 6 times (curve 3) and the specific capacity does not change, suggesting that this electrode is regenerate and can be reused as cathode in sodium ion batteries.

3.1.5 Electrochemical Impedance Spectroscopy.

In order to have a deep insight into the kinetics of the sodium ion insertion and extraction, Electrochemical Impedance Spectroscopy (EIS) data were collected at different potential. Figure 22 shows the Nyquist plots for CsNaZnHCF at the following potentials: 0.7, 0.81 and 0.95 V/NHE (Figure 22A) during charge process and at 0.93 and 0.8 V/NHE (Figure 22B) for the discharge. All the plots are formed by a semicircle in the high frequency region, followed by a poorly defined response and a straight line at intermediate and low frequency regions, respectively. The high frequency response corresponds to the charge transfer process and the low frequency feature senses the cation diffusion process through the hexacyanoferrate framework. The appearance of a well-defined straight line with a slope greater than 45 degrees in the plots suggests that the cation diffusion, related to its insertion and release, is of finite type and it is dominant process for the electrochemical reaction on the electrode. It is evident that the slope in the straight line increases to more cathodic potential, but without major changes in the semicircles at high frequencies (see Figure 22, Inset).
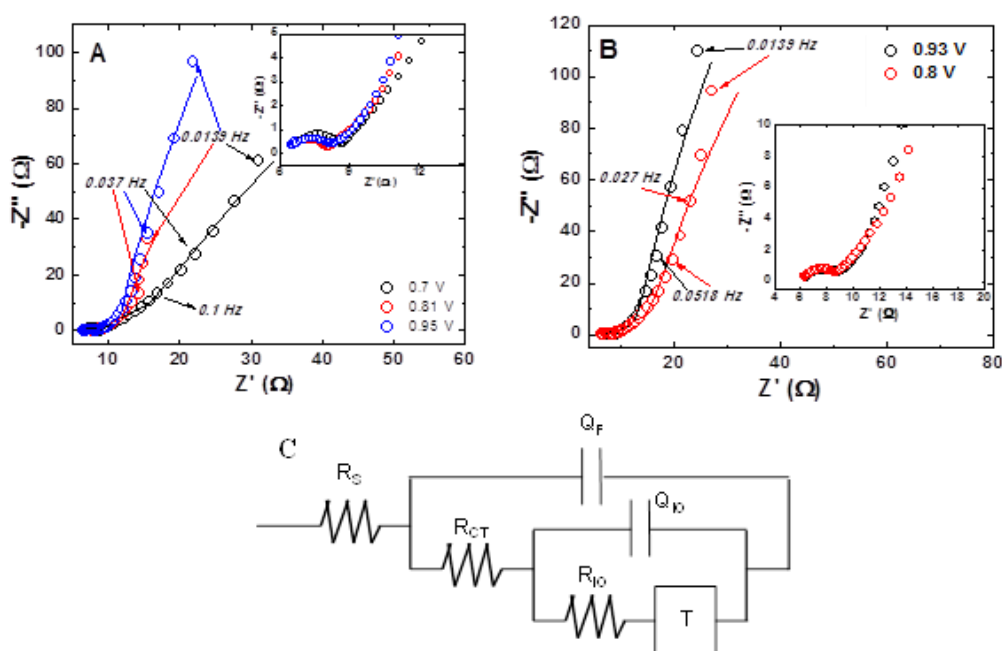
Figure 22. Nyquist plot of CsZnHCF in NaNO$_3$ at different potential (A) during oxidation, (B) during reduction and (C) equivalent circuit.

The EIS plots were modeled by an equivalent circuit (Figure 22), where R_S is the solution resistance; Q_F is a capacitive phenomenon due to the capacitance of the electrode; R_{CT} is the charge transfer resistance of the electrochemical reaction; Q_{RIO} is assigned to the ionic transfer resistance, while the finite cation diffusion inside the framework is attributed to T element.

Due to irregularities in the surface of materials, constant phase elements (Q) were used. Such least square fitting according to an equivalent circuit and the nomenclature used were carried out according to Boukamp[53]. The obtained fitting is shown by solid lines in Figure 22, where an excellent correlation with experimental data is appreciated. The values for Y_O and B parameters were obtained from the diffusion element T. R_S remains constant around 6 Ω, as expected because solution composition and thus conductance do

not change. To more cathodic potential, the value of R_{CT} exhibits small increments, whereas R_{IO} decreases because the charge transfer in the framework depends to the cation diffusion inside the cavity. In order to shed light to this model, the diffusion coefficient was calculated using the approaches reported by Boukamp[53]. These approaches suppose the existence of certain correlation between kinetic parameters and electrical elements obtained by the fitting of experimental data using equivalent circuits. The diffusion coefficient (D) can be estimated according to the following equations:

$$Z(w) = \frac{Z_O\,Coth(B\sqrt{jw})}{B\sqrt{jw}} \quad\text{...(4)}$$

$$Z(o) = \frac{lV_m}{FsD_{z^+}}\left[\frac{dE}{d\delta}\right] \quad\text{...(5)}$$

$$B = \frac{l}{\sqrt{D_{z^+}}} \quad\text{..(6)}$$

where l: is the film thickness (0.8 μm obtained by VeecoDektak3 Surface profilometer); V_m: molar volume of CsZnHCF (445.57 cm^3 mol^{-1} obtained from reference 15); F: Faraday constant (96486 C mol^{-1}); s: active surface area in cm^2, and D_{z^+} is the diffusion coefficient in cm^2 s^{-1}.

In this work, the equivalent circuit, allows us obtaining the B parameter, which is related to the value of D according to equation 6. The calculated values for D, summarized in Table 4, are in the order of 10^{-9}, which is one order of magnitude lower than the sodium diffusion coefficient (10^{-8}) reported recently and in the same order of magnitude reported for potassium ions diffusing through cupper (II) hexacyanoferrate (II). This permit to confirm that faradaic process observed in the electrode CsNaZnHCF are due to Cs$^+$ cation mobility during insertion/desertion process.

Table 4. Diffusion Coefficient of Cs^+ at different potential in ZnHCF

E (V)	Thickness (cm)	B (seg$^{1/2}$)	D_z^+ (cm^2 s^{-1})
0.7	8 x 10^{-5}	1.961	1.664 x 10^{-9}
0.81	8 x 10^{-5}	1.886	1.8 x 10^{-9}
0.95	8 x 10^{-5}	1.129	5.021 x 10^{-9}
0.93	8 x 10^{-5}	1.16	4.756 x 10^{-9}
0.8	8 x 10^{-5}	1.507	2.818 x 10^{-9}

3.2 Non-aqueous Media

Recently revealed by Goodenough's group that electrochemical properties of $Na_{2-x}Mn[Fe(CN)_6]\cdot zH_2O$ with Monoclinic phase are improved by interstitial water removal, due to a structural change to Rhombohedral phase[46], which delivers 150 mAh g^{-1} with flat charge and discharge plateaus at 3.5 V, whereas, Yang et. al. reported the synthesis of Prussian Blue-reduced graphene oxide composite (PG-RGO) from coordinated water removal in PG where the oxide group in GO accept one electron from Fe^{2+} (HS) which has coordinated water due to $[Fe(CN)_6]^{n-}$ vacancies, enhance the specific capacity and stability[54]. However the critical effect of interstitial water inside to hexacyanoferrate has not yet been completely understood.

3.2.1 Structural Characterization

Figure 23A shows the experimental XRD pattern of o-ZnHCF and m-ZnHCF respectively (red line); the diffraction patterns were fitted by Le Bail method (black line). The anhydrous solid, D-NaZnHCF, crystallizes with a monoclinic unit cell in the P2/c space

group, revealing that the thermal treatment on NaZnHCF induces a structural transition as has been reported by Avila and co-works[50].

To understand the electrochemical results discussed below, the structure of the frameworks are exhibited in Figure 23B, which was drawn using Diamond software.
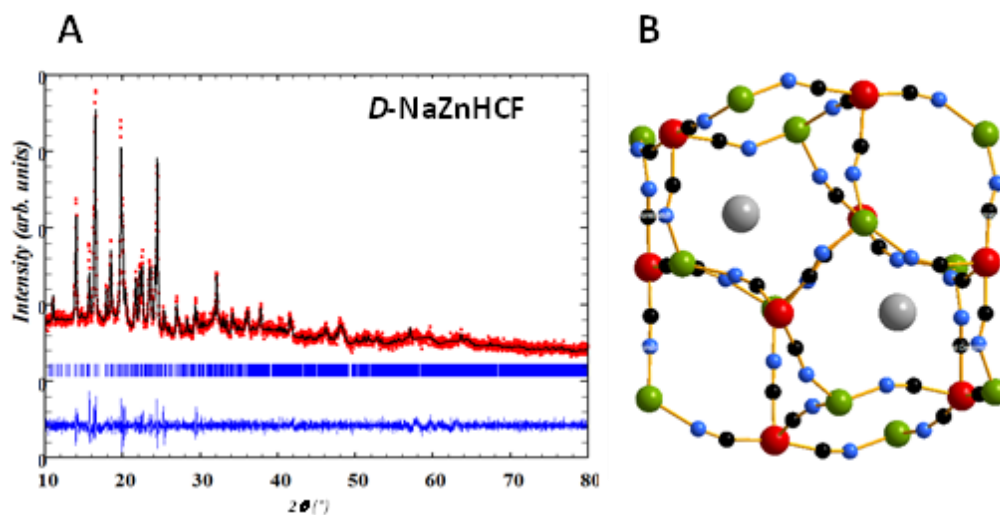

Figure 23. Powder XRD pattern, with a Le Bail profile fitting for the materials under study; porous framework for Zinc Hexacyanoferrate without water. A given cavity accommodates two Na^+ cations (gray spheres). The framework negative charge is accumulated on the N atom (blue sphere) coordinated to Zn atom (green spheres). C atom (black sphere) is coordinated to Fe atom (red sphere).

After water removal by heating, in *D*-NaZnHCF the sodium ion migrates towards the N ends in order to maximize the attractive electrostatic interaction between Na^+ and framework structure, by increasing the Na^+-Na^+ separation within the structure [50], inducing a stronger interaction between sodium and framework and reducing the CN ligand ability to donate charge to the Zn atom; modifying the bond distances and angle accompanied by a volume cell contraction of about to 12% due to a charge redistribution, (Fig. 23B). Under such conditions, the sodium ion mobility within the frameworks only take place between N end from neighboring tetrahedron [51]. The Figure 24 shows the FTIR

spectrum of hydrated (NaZnHCF) and dehydrated (*D*-NaZnHCF) sample. The frequency for

v(CN) stretching vibration around of 2090 cm^{-1} for NaZnHCF indicates only the presence of

Fe^{II} in the structure, this vibration increases by 6 cm^{-1} in *D*-NaZnHCF, with a notable peak

splitting. Such behavior is assigned to a pronounced decrease on the local symmetry

around the N end, removing the degenerating character of this vibration due to high

polarizing power of sodium ion which increases a charge subtraction at the nitrogen end

through the 5σ orbital [50], which is a sensor for the stronger Na$^+$-framework interaction in

D-NaZnHCF.
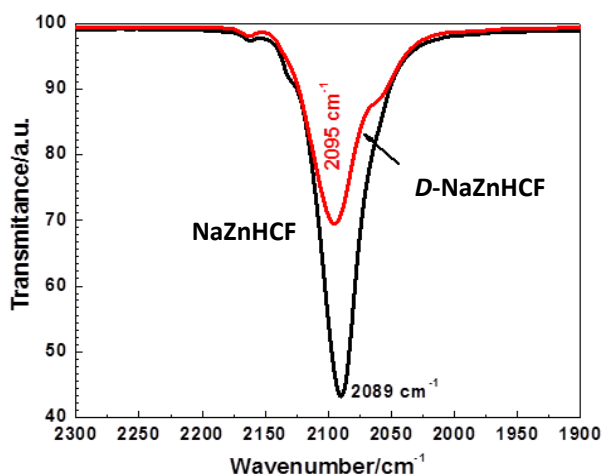
Fig. 24 Infrared Spectroscopy of NaZnHCF and *D*-ZnHCF.

3.2.2 Electrochemical evaluation

To our best knowledge, there are no reports on Cyclic Voltammetry (CV) measurements in

these systems. The Figure 25A exhibited the CV at 0.1 mV s^{-1}, started at open-circuit

potential (OCP) in the anodic direction. *i-E* characteristic of curves for both samples

exhibited two faradic processes, the first process shows wide peaks suggesting a possible

ohmic drop effect and a possible IR compensation is necessary, however, the thin and defined peak in the second process indicates that electrochemical profiles are not affected by ohmic drop. The peak to peak separation ($\Delta E_p = E_{pa} - E_{pc}$) where E_{pa} and E_{pc} are the positions of the anodic and cathodic peaks, respectively, shown in Table 5, reveals that process *II* has a better electrochemical reversibility than process *I* in both materials. The E_f calculated according to $E_f = (E_{pa} + E_{pc})/2$; exhibited that *D*-NaZnHCF is higher by 100 mV than in NaZnHCF for peak *I*; whereas, in the peak *II* the E_f of NaZnHCF becomes higher by 60 mV than in *D*-NaZnHCF.

Table 5. Summary of results from cyclic voltammetry curves for the materials under study

	Peak *I*		Peak *II*	
	NaZnHCF	*D*-NaZnHCF	NaZnHCF	*D*-NaZnHCF
ΔE_p/mV	310	360	296	240
E_f/V	3.20	3.30	3.80	3.74

On the other hand, Galvanostatic charge/discharge experiments were performed at c/10, which is shown in Figure 25. Both samples exhibited a process between 3.2-3.65 V vs Na^+/Na, where the sodium amount is high, the potential change according to specific capacity increases. This behavior is associated to a solid solution formation [55]. Whereas at 3.7 V vs Na^+/Na where the sodium amount is low, it is evident a flat process attributed to phase transition [55a, 56]. It is evident that *D*-NaZnHCF exhibited a high reversibility at c/10, whereas, the specific capacity for NaZnHCF is 55 mAh g^{-1}. For *D*-NaZnHCF, it is 64 mAh g^{-1}; which is very closed to theoretical capacity of 64.8 mAh g^{-1} for these framework structure, where only the iron present in octahedral $[Fe(CN)]_6^{n-}$, is the electroactive specie.

A small improvement on the rate capability (see inset in Fig. 25B) at different C-rate is observed in *D*-NaZnHCF.
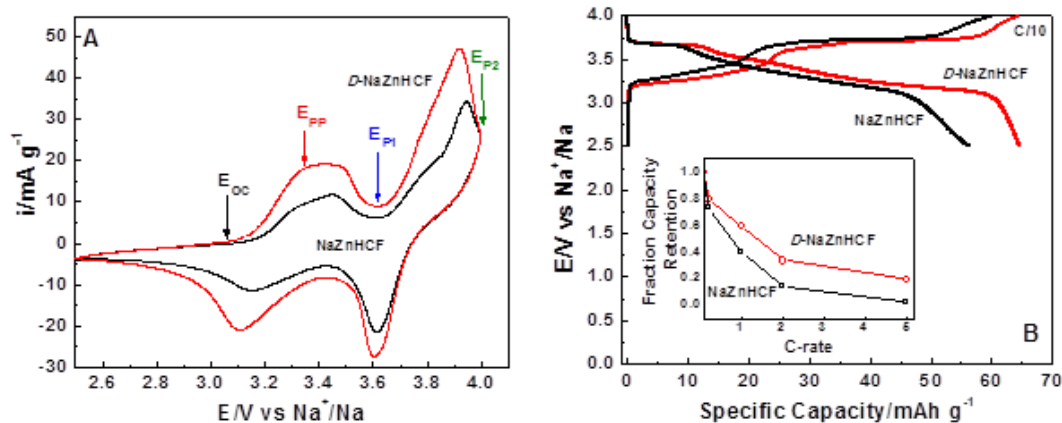

Figure 25. A) Cyclic Voltammetry at 0.1 mV s^{-1} and B) Galvanostatic charge/discharge at c/10 rate, inset: fraction capacity retention at different C-rate.

3.2.3 Electrochemical Impedance Spectroscopy

The Figure 26 shows the Nyquist plots obtained from the Electrochemical Impedance Spectroscopy (EIS). The EIS were performed up to different potentials (open circuit potential (E_{oc}), pre-peak potential (E_{PP}), after process 1 potential (E_{P1}) and after process 2 potential (E_{P2}) see figure 25), which was reached after a linear Sweep Voltammetry at 0.1 mV s^{-1}, followed by OCP measurement by 30 minutes. In general, all Nyquist diagrams present similar characteristics. *o*-ZnHCF shows, at higher frequencies, a wide semicircle indicating the contribution of two processes with similar time constants (Fig. 26A). Those processes are better defined on the Nyquist diagram of *D*-NaZnHCF indicating more dissimilar time constants (Fig. 26B), i.e. water removal induces changes on the frequency response of these processes [57].
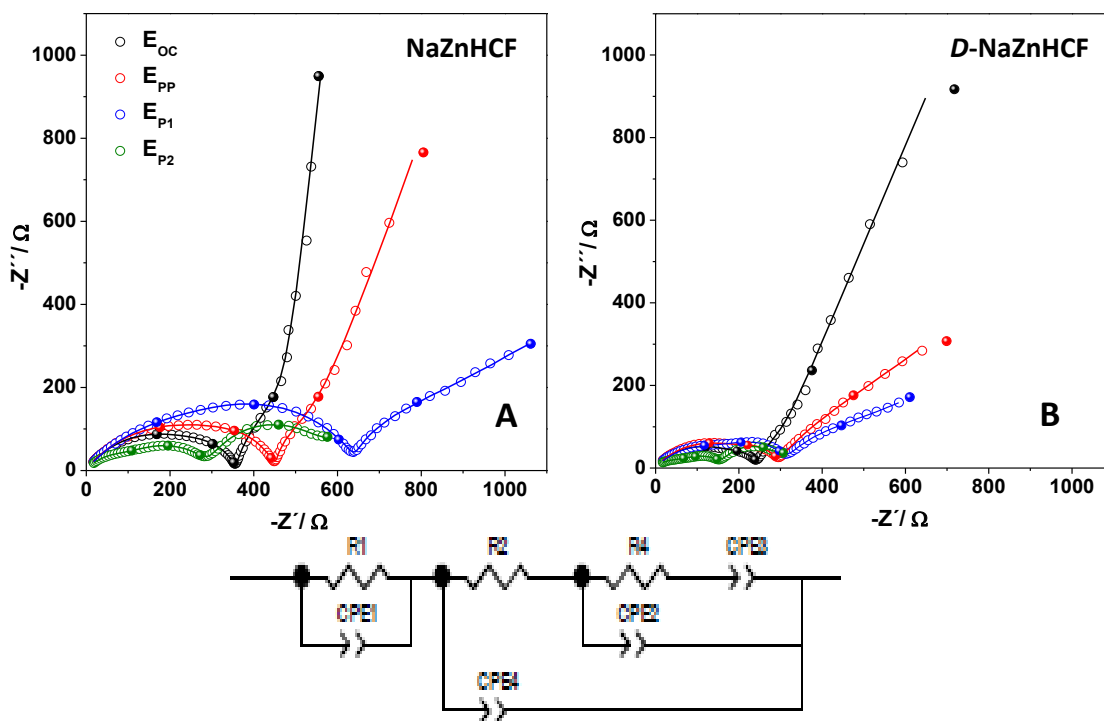
Figure 26. Nyquist plot at different potential and Equivalent circuit obtained from fitted of Electrochemical Impedance Spectroscopy.

It has been reported that this phenomenon can be attributed to charge transfer, which depends of: *i*) the electronic conduction; and *ii*) ionic conduction, occurring under synchronic conditions. After the semicircles, at lower frequencies, in the Nyquist diagram, the presence of a well-defined straight line with two slopes is evident (see black points of Nyquist diagram in Fig. 26). The changes in slope of the straight line suggests cation diffusion changes from finite type at medium frequencies to semi-finite type at low frequencies [58]. In general, in both materials, an increase in the semicircle size is observed when the applied potential is higher. On the other hand, as the applied potential is higher, a decrement on the slope of the straight line at low frequencies is observed, indicating that the diffusive process of Ion is being facilitated. The presences of well-defined straight

line at medium and low frequencies are inhibited at E_{P2} (green diagrams in Figure 26), so the change on the characteristics of the Nyquist diagram is related to adsorptive phenomenon[59].

The equivalent circuit illustrated in Figure 26C was employed to analyzed the EIS results. The electron transport throught the hexacyanoferrate lattice is defined by the parallel combination of the resistance $R1$ and constant phase element $CPE1$, the ionic conduction, which takes place along the electron transfer by a hopping mechanism, is described by the parallel combination of the resistance $R2$ and $CPE4$; whereas the $R3$, $CPE2$ and $CPE3$ at low frequencies are associated to diffusion processes during sodium insertion/desertion. The values obtained from the fitting are exhibited in Table 6.

Table 6. Resistance values obtained from equivalent circuit.

	E	R1	R2	Chi-squared
NaZnHCF	E_{OC}	307	55.06	9.05E-05
	E_{PP}	380.7	78.85	9.04E-05
	E_{P1}	328.8	329.4	5.20E-05
	E_{P2}	107.5	194	3.68E-05
D-NaZnHCF	E_{OC}	204.4	49.58	0.00042984
	E_{PP}	233.7	70.65	9.19E-05
	E_{P1}	189.5	140.3	9.11E-05
	E_{P2}	64.23	104.3	8.84E-05

The calculated resistances in NaZnHCF are higher than in D-NaZnHCF, particularly in R1 and R2 indicating that a better charge transfer in D-NaZnHCF; in both samples the highest

value of $R1$ is observed at E_{PP}, whereas the resistance to cation conduction ($R2$) is highest at E_{P1}.

As was mention above, in these materials only the iron the molecular block $[Fe(CN)_6]^{n-}$, can participate in redox processes during electrochemical processes, so that, the two Faradic processes mentioned above have different Na-ion insertion/desertion mechanisms. The first Faradic process associated to solid solution occurs at a high sodium concentration in the structure as has been reported for this kind of open framework materials[33]. The sodium diffusion is constant through the framework channel, so that the Faradic process depends mainly on the electron diffusion through the lattice as was demonstrated by EIS results where $R1$ at E_{pp} is highest. A higher value of E_f in D-NaZnHCF, with respect to NaZnHCF, can be associated to the high polarizing power effect of sodium over N ends in the framework in D-NaZnHCF, as it was observed by IR results, increasing the charge subtraction over iron low spin through the π-back donation mechanism. This produces a decrease in the absolute energy of the fully filled t_{2g} orbitals, hence favoring the 2+ oxidation state in iron[52]. Therefore, the applied potential (E_f) for sodium desertion to occur increases. The lower electrochemical reversibility in NaZnHCF can be attributed to effect of cell contraction exhibited in the monoclinic phases.

The charge of the first peak represents the third part of the total charge of the electrochemical processes (calculated from CV at invertion potential E_{p1} and E_{p2}), indicating that only approximately 0.6 mol of cations are involved, producing on the interface the system $Na_{2-x}Zn_3[Fe^{II}(CN)_6]_{2-x}[Fe^{III}(CN)_6]_x$, which can be associated to the presences of two phases one sodium rich and one sodium poor, where the sodium should

be re-located inside the structure with the aim to maintained the electric neutrality in the framework; both phases have the same crystal structure but with different electronic properties due to the presences mixed valance state of Fe^{III}/Fe^{II} as has been reported by $LiFePO_4$[56, 60]; the presences of this two phases on the interface promotes a different mechanism of Sodium Insertion/desertion associated to phase transition behavior in the second faradic process. Which can be related to sodium mobility within the framework, this explain that resistance assigned to cation conduction ($R2$) in the framework is higher at E_{P1}, in NaZnHCF the water promotes a notable higher resistivity for the sodium mobility due to presences of compact network of water molecules within the porous increasing the interaction between water and sodium remains more strongly linked to the solid[51] specially in sodium poor phase where only there are one Na in the cavity, this cation mobility induce the electron hopping on the lattice for this reason the E_f and ΔE_P is lower in D-NaZnHCF.

3.2.4 Diffusion Study

Figure 27, shows the galvanostatic intermittent titration technique (GITT) experiments, in the rage of 2.5-4.0 V vs Na^+/Na. GITT was employed at a pulse of C/10 for 10 min followed by a 30 minutes of interruption between each pulse to allow for full relaxation at the open circuit potential and reach a stabilized potential value. From the GITT the diffusion coefficient during insertion/desertion of the sodium ions (D_{Na^+}) in the host can be effectively determined using the Fick's second law of diffusion [61].

$$D_{Na^+} = \frac{4}{\pi}\left(\frac{m_B V_m}{M_B S}\right)^2 \left(\frac{\Delta E_s}{\tau\left(\frac{dEr}{d\sqrt{\tau}}\right)}\right)^2 \qquad \left(\tau \ll \frac{l^2}{D_{Na^+}}\right) \quad \text{...(7)}$$

Where m_B, V_m, M_B and l are the mass, the molar volume, the molecular weight and the thickness of the electrode material, respectively, and S is the surface area of the electrode; the molar volume (V_m) for o-ZnHCF and m-ZnHCF are 448.71 cm^3 mol^{-1} and 392.097 cm^3 mol^{-1}, respectively and is assumed to remain stable during charge/discharge process, and it was calculated based on the reported data.

The results reveals that D_{Na^+} is modified during charge/discharge process, during sodium desertion in first process (between 3.2-3.65V) the D_{Na^+} decrease from 8 x 10^{-9} to 3 x 10^{-11} cm^{2}s^{-1}, this can be associated to that sodium mobility inside the structure decrease by the progressive formation of Fe^{III} inhibiting the jumps of sodium on the N ends in the chain Fe^{III}-CN; whereas in the second process is observed a rapid increase and decrease in D_{Na^+} until reach a diffusion value near 3 x 10^{-13} cm^{2}s^{-1} due to during phase transition the Na$^+$ mobility in sodium poor phase decrease.

Evident differences are observed in three step in the electrochemical process, near to 3.4 V vs Na$^+$/Na the D_{Na^+} is 7.4 x 10^{-11} and 6.9 x 10^{-12} cm^{2}s^{-1}, whereas the D_{Na^+} close to total desertion of the sodium ion are 2.04 x 10^{-12} and 4.39 x 10^{-13} cm^{2}s^{-1}; during sodium insertion the most important difference in D_{Na^+} can be detected close to total discharge process 1.84 x 10^{-12} and 4.17 x 10^{-13} cm^{2}s^{-1} in every step the m-ZnHCF exhibited a better D_{Na^+} verify the discuses before about to sodium mobility within the framework.

This sodium diffusion also can be related to change in free energy (ΔG_{Na})[62]; as in o-ZnHCF the ΔG_{Na} is higher due to the presences of coordinated water with sodium inside the framework, whose exhibited a higher free energy of "hydration" ΔG_h= -365 kJ mol^{-1} [63] than solvation energy (ΔG_s) in dimethyl carbonate (DMC)/ethylene carbonate (EC), ΔG_s= -

300 kJ mol^{-1} for EC and -190.7 kJ mol^{-1} for DMC [64]; whereas in *m*-ZnHCF this *ΔG$_h$* is not present decrease the *ΔG$_{Na}$*, promoting that during sodium insertion/desertion the changes in solvation/desolvation energy not affect the structure stability; explaining the improve in capacity retention.
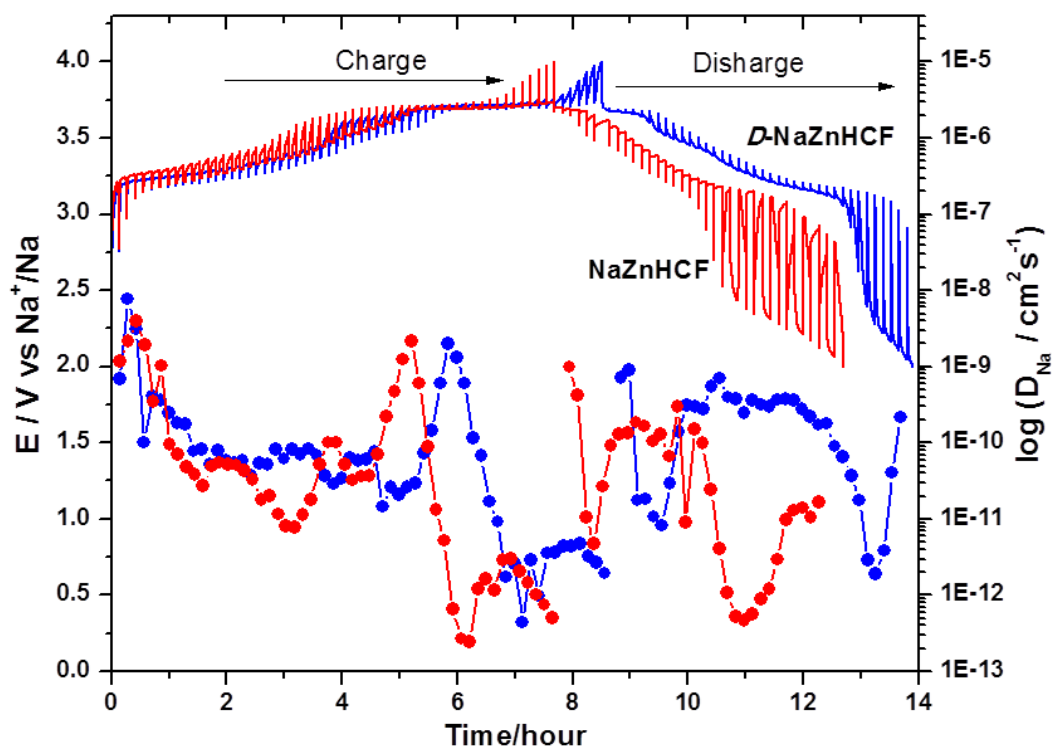

Figure 27. Galvanostatic intermittent titration and sodium diffusion coefficient In function of time.

3.3. Conclusions

The electrochemical behavior of ZnHCF was evaluated in aqueous and non-aqueous media. The modification of cationic mobility within the structure is essential to improve the charge retention at different cycles and at different *C*-rate.

For aqueous media, the material electrochemical features are dominated by the exchangeable cation polarizing power and the solvation energy in the solution. When the experiment is carried in solution of $NaNO_3$, the cation in the structure (K^+ and Rb^+) is progressively replaced by Na^+, which was ascribed to a higher mobility for this last one. For Cs^+, the structure high affinity for this cation results in the formation of a mixed composition $Zn_3NaCs[Fe(CN)_6]_2xH_2O$. This cation exchange ability permits to use of ZnCsNaHCF as cathode in aqueous sodium ion batteries, with the possibility their reused after capacity retention decrease.

For non-aqueous media, the sodiation/desodiation processes occur by two different mechanisms in function of the applied potential, whereas the presence of water within the framework has effect on the charge subtraction promoting by sodium on the Fe through the N ends of the cyanide ligand, affecting the first Faradaic process, and the sodium mobility exhibits an important influence on the second redox process. The water removal also affects the sodium mobility inside the structure improving the sodium diffusion in D-NaZnHCF during charge/discharge, enhancing the specific capacity and the rate capability at higher C-rates.

CHAPTER 4.

4. Results and Discussion (M-Manganese Hexacyanoferrate, M:Fe,Ni,Co)

4.1 Aqueos Media

Recently Pasta et. al.[65] reported the synthesis of $Na_{2y}Co_{1-x}Mn_x[Fe(CN)_6]_y$ using an excess of sodium during precipitation reaction, with the purpose to decrease the amount of Co in the framework to obtain a low cost material. However, the results revealed that Jahn Teller distortion exhibited by Mn^{3+} decrease the stability during Faradic process in aqueous media.

4.1.1 Structural Characterization

The chemical composition calculated by OES-ICP of every sample and their labeled is exhibited in Table 7. All samples showed a high amount of sodium and an a Mn/Co or Co/Fe ratios closed to 1, indicating that structure has a low amount of vacancies by $[Fe(CN)]^{4-}$.

Table 7. Chemical Composition and Mossbauer values

Sample	Formula	IS (mm/s)	QS (mm/s)
CoHF	$Na_{1.84}Co[Fe(CN)_6]_{0.96}$	-0.1894	0.1841
CoMnHF3	$Na_{1.88}Co_{0.8}Mn_{0.2}[Fe(CN)_6]_{0.97}$	-0.1897	0.1872
CoMnHF2	$Na_{1.88}Co_{0.55}Mn_{0.45}[Fe(CN)_6]_{0.97}$	-0.1903	0.1932
CoMnHF1	$Na_{1.88}Co_{0.3}Mn_{0.7}[Fe(CN)_6]_{0.97}$	-0.1908	0.1952
MnHF	$Na_{1.92}Mn[Fe(CN)_6]_{0.98}$	-0.1911	0.1972

The XRD pattern was adjusted by Le bail fitting method (Fig. 28). The fitting shows that every material crystallize with a monoclinic cell in the $P2_1/n$ space group. The distortion of classic cubic cell is due to high amount of sodium in the structure produced by the use of citrate-chelating method, which decreases the reaction kinetics in the formation of the hexacyanoferrate[66]: The Na^+ ions prefer to stay asymmetrically at the N-coordinated corners with much closer Na−N distances, which induces a distortion of an elementary cell (inset in Fig 1), associated to a cooperative displacement of the $(NaOH_2)^+$ groups in alternating cubic [111] and [1-11] direction[67].
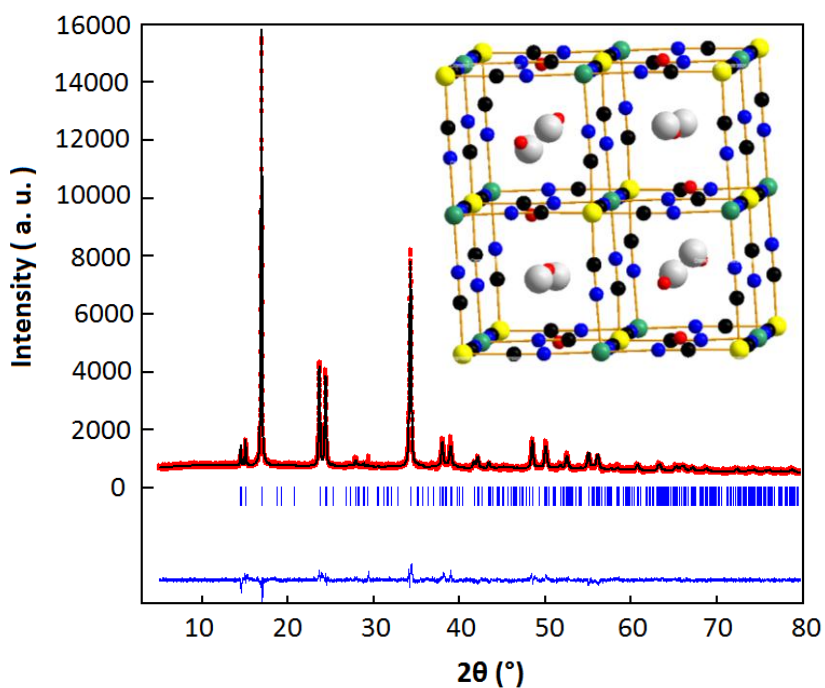

Figure 28. Powder XRD, with a Le Bail profile fitting for the materials under study, inset: Crystalline structure, where Na+ cations (white spheres), oxygen from eater (red spheres). The framework negative charge is accumulated on the N atom (blue sphere) coordinated to Co/Mn atom (green spheres). C atom (black sphere) is coordinated to Fe atom (yellow sphere).

The C≡N⁻ ligand has the ability to act as a σ-donor by donating electron charge to the metal coordinated to N end. This electron subtraction occurs through the 5σ orbital which has certain anti-bonding character for the CN group. The metal coordinated to C end exhibited the π bonding interaction which involves the t_{2g} electrons of metal with the π and π* orbitals of the ligand[68]. This phenomenon permits to sense the oxidation state of internal and external metal in cyano complex by Infrared (Figure 29A) and Raman spectroscopy (Fig. 29B).

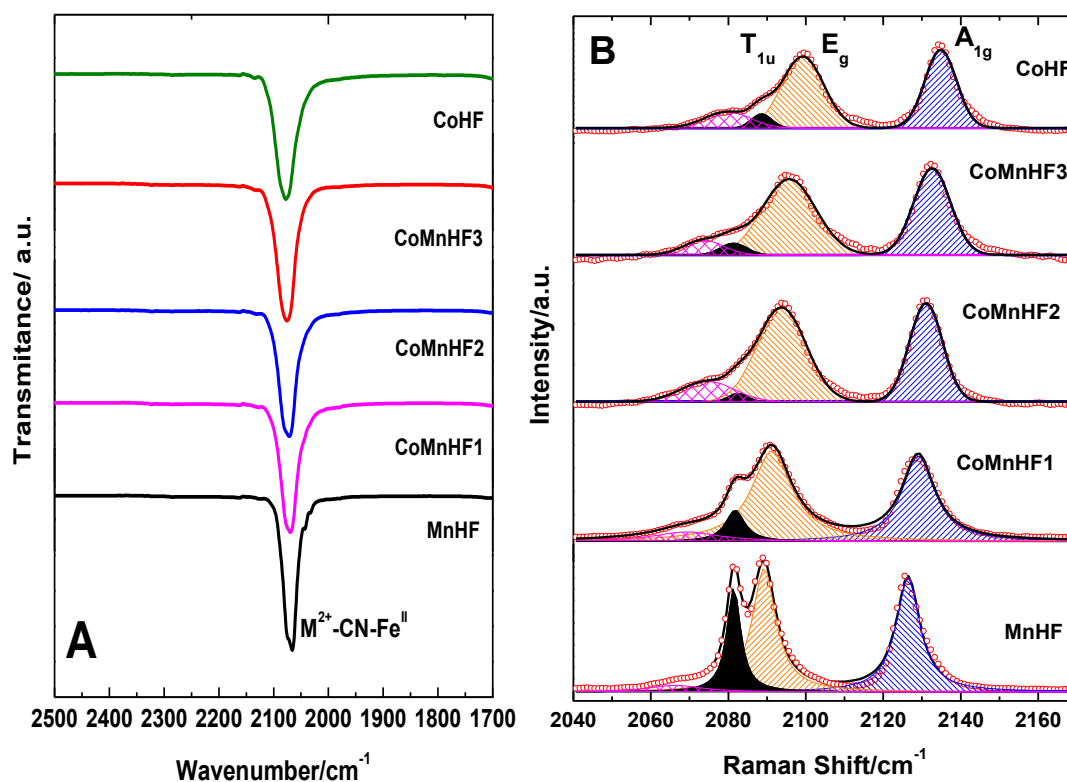Figure 29. A) Infrared and B) Raman Spectrum

The FTIR spectrum of every materials reveals a band c.a. 2070 cm⁻¹ assigned to M^{2+}-CN-Fe^{II} links, the substitution of Mn^{2+} (Z/r^2= 3.287) by Co (Z/r^2= 3.652) in the structure promotes

that ν(CN) stretching vibration increase, due to the polarizing power (Z/r^2) of cobalt increases a charge subtraction at the N end through the 5σ orbital; the splitting in the ν(CN) vibration in MnHF is evident. This can be associated to a decrease in the local symmetry around the N end. The Fe cation in haxacyanoferrates materials present a local O_h point group symmetry with an inversion center and exhibite two stretching modes A_{1g} and E_g[69]. The vibration modes A_{1g} appears near to 2128 cm^{-1}, whereas at 2095 cm^{-1} the E_g mode is observed verifying the presence of M^{2+}-CN-Fe^{II} links in all sample[70]. The band near to 2080 cm^{-1} can be associated to T_{1u} vibration, indicating a localized structural distortion provoking deviations from ideal O_h symmetry to D_{4h} symmetry[69]. It has been reported that this band (T_{1u}) can be splitted in two contributions[71], which explains the presence of band at lower Raman shift (pink contribution).

The room temperature ^{57}Fe Mössbauer spectra are shown in Figure 30. The low value of isomer shift ($IS≈$ -0.19 mm/s) is assigned to Fe^{II}-C low spin (LS) with electronic configuration $t_{2g}^6 e_g^0$, which exhibites only a singlet due to d electrons are filling the t_{2g} levels ($S=0$). So, no electric field gradient exists causing no quadrupole splitting (QS) takes place[72]. However, the results in this paper exhibited quadrupole splitting ($QS≈$ 0.19 mm/s). This can be interpreted as a charge anisotropy due to an important distortion in the environment of the octahedral[70b] [Fe(CN)$_6$]$^{4-}$ moiety, as was observed by Raman. The IS and QS decrease with respect to Mn is substituted by Co in the Framework (Table 7), indicating that the amount of 3d electrons on the iron atom and their shielding effect on the S electrons density at the iron nucleus, lowering their value. This is due to the cobalt with higher polarizing power increase the charge substation over N ends promoting an

increase in the π-back donation from the iron atom towards the CN ligand, and that the
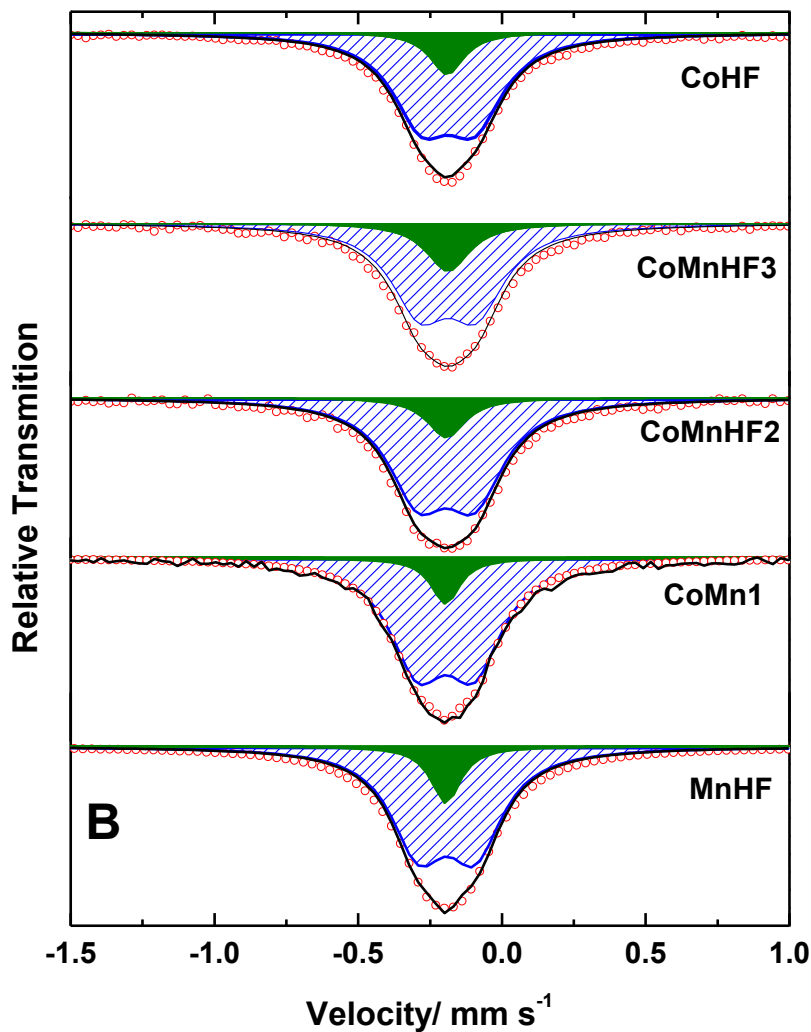
cell distortion is promotes by Manganese presence.

Figure 30. [57]Mossbauer Spectrum

The manganese and cobalt interaction in the structure was analyzed by EPR

measurements (Fig 31). All the EPR spectra of CoMnHF compounds shown a singlet signal

with an average line width of 20 gauss, with the exception of the CoHF compound which is

EPR silence.

The Mn coordinated to N exhibited electronic configuration in high spin $t_{2g}^5 \, e_g^2$ with $S=5/2$, so that in EPR experiments three Kramer's doublets, $\pm 5/2$, $\pm 3/2$ and $\pm 1/2$ are expected, however, at room temperature (Fig. 31A), the compound MnHF has a broad singlet EPR signal with a $g= 2.023$, this is due to applied magnetic field, which removes the degeneracy of such doublets and the EPR spectra are coming from transitions between energy levels of the Kramer's doublets. The resonance at $g=2$ arise from transition between energy levels of $S= 1/2$ Kramer's doublet.

A very probable possibility by which only the transition of the ground doublet ($\pm 1/2$) appears is that exited doublets ($\pm 5/2$ and $\pm 3/2$) are populated; then the lifetimes of the exited estates are generally so short because of relaxation to the lattice that transitions between them are too broad to be observable. So that in practice resonance is almost always restricted to the ground doublet[73]. In the EPR profile no resolved hyperfine structure. The shape and line width of that signal implies that there are a dipole coupling and an interchange interaction. This behavior can be associated to ferromagnetic interaction, indicating that two magnetic orbitals are orthogonal, and then the ground state of the system has parallel electron spins (Hund's rule).

In contrast, the CoHF compound did not show EPR signal, which implies an antiferromagnetic ordering of the spins ($S= 3/2$) of the Co^{2+} ions. This antiferromagnetic behavior in nature is a consequence of the Pauli principle, leading to an antiparallel spin ordering where two magnetic orbitals are not orthogonal[74].

The magnetic coupling of metals in hexacyanometalates is explainable neither by dipole-dipole interactions nor by direct exchange interactions via overlapping metal orbitals. The coupling may be described in terms of a superexchange mechanism through the cyanide ligands[74] between two neighboring metals. However, in this samples the iron center has S= 0 exhibited a diamagnetic behavior, so that the magnetic interaction can be associated to valence delocalization mechanism as has been reported by Prussian Blue[75]; where the electron occupied in orbitals t_{2g} in Fe^{II} are partial delocalized on to neighboring (Co/Mn). For MnHF the Mn^{2+} (t_{2g}^3 e_g^2) where the t_{2g} and e_g orbitals are both exactly half occupied, a t_{2g} electron with a fraction of spin from Fe^{II} can interact with electrons in e_g orbitals in Mn, promoting that the spin is ordered parallel to each other. Whereas for CoHF with a Co^{2+} (t_{2g}^5 e_g^2) the interaction occurs in t_{2g} orbital provoking that the spin is ordered antiparallel to each other.
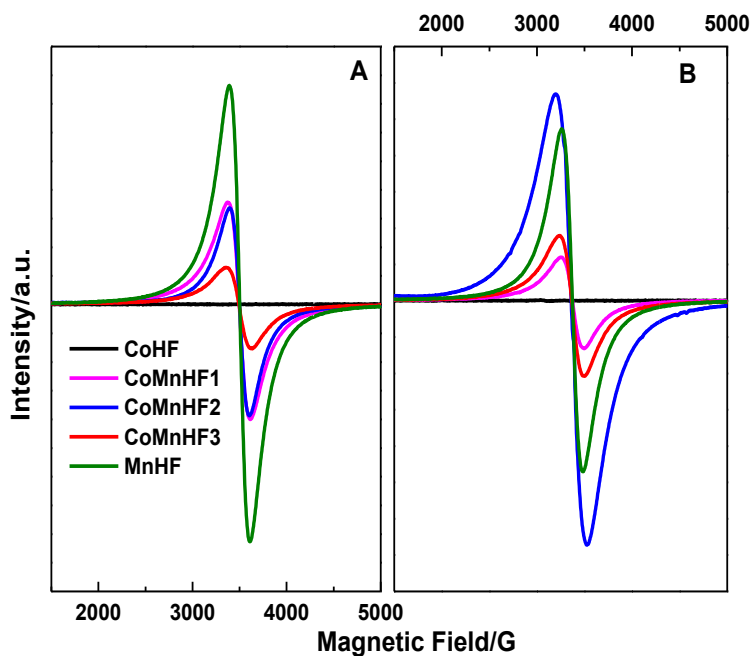

Figure 31. Electronic Resonance Paramaganetic A) at room temperature and B) at 77K.

On the other hand, as the Co concentration decreases, the EPR spectra intensity increases until to obtain a maximum intensity for MnHF. This increase is not monotonically, since CoMnHF1 and CoMnFH2 have practically the same intensity (see Figure 31A). In order to investigate a few more about the mechanisms that might be involved in the evolution of the EPR spectra when the Co (or Mn) concentration is varied, the CoMnHF compounds were measured at 77 K (Fig 31B). The EPR behavior for the CoHF and MnHF compounds is very similar to that described for these same compounds at 300 K. However, for the CoMnHF1, CoMnFH2 and CoMnFH3 compounds abrupt changes occur in the intensity of their respective EPR spectra.

In particular, for the CoMnFH2 compound the intensity of its spectrum is greater than that of MnHF compound. This implies that the number of paramagnetic entities contributing to the EPR signal has increased considerably. Suggesting that spin of cobalt are ordered in parallel due to cation arrangement of both Co and Mn metals in the frameworks, where the Fe^{II} is probably surrounded by three Co^{2+} and Mn^{2+}, presented the chain Co-NC-Fe-CN-Mn, where the cobalt induces a higher charge subtraction on iron modify the spin delocalization.

4.1.2 Electrochemical Evaluation

The Cyclic voltammetry of every material at 1 mVs^{-1} in 1M $NaNO_3$ (Fig. 32A); the CoHF exhibit two faradic processes the first at formal potential (E_f = 0.35 V vs Ag/AgCl) is attributed to electrochemical process of redox couple Co^{3+}/Co^{2+}, this is accompanied of a change in the electronic configuration, from high (HS: $t_{2g}^5 e_g^2$) to low spin (LS: $t_{2g}^6 e_g^0$), due

to the e_g^0 orbitals in Co^{3+} (LS) are free, has the ability in the chain Co^{III}-CN-Fe^{2+} to subtract electron from CN ligands mainly from their 5σ orbitals, increase the redox potential associated to Fe^{III}/Fe^{II} redox couple (E_f = 0.87 V vs Ag/AgCl), the anodic peak at 0.43 V vs Ag/AgCl is associated to Na-ion desertion along the (111) directions, during oxidation process, which induces a structural changes in unit cell from monoclinic to cubic, the peak to peak separation for Fe^{III}/Fe^{II} redox couple is ΔE_p= 60 mV indicating a good electrochemical reversibility, whereas the ΔE_p= 100 mV is observed in Co^{3+}/Co^{2+} redox couple this semi-reversible process due to the stability of Co^{3+} LS configuration ($t_{2g}^6 e_g^0$), where a transfer of charge density from the t_{2g} to e_g orbitals should take place, this can be very by the electrochemical profile observed between 0.55-0.75 V/ vs Ag/AgCl which has been attributed with a gradual rearrangement of the electronic structure during Co^{3+} (LS)/Co^{2+}(HS) redox process[65]. Any change was observed in the electrochemical profile for 50 cycles. On the other hand, the MnHF shows during anodic sweep a faradic process at 0.52 V vs Ag/AgCl (thin line), attributed to oxidation of Fe^{II} ($t_{2g}^6 e_g^0$) to Fe^{III} ($t_{2g}^5 e_g^0$), due to spontaneous hopping electro from Mn to Fe through the cyanide linker as has been reported [65]; the structural changes during sodium extraction take place at 0.58 V vs Ag/AgCl, the anodic peak at 1.1 V vs Ag/AgCl may be associated to Manganese oxidation from Mn^{2+} ($t_{2g}^3 e_g^2$) to Mn^{3+} ($t_{2g}^3 e_g^1$), which present the Jean Teller distortion contributing to structural strain in the lattice and decrease the stability, this explains that during the cathodic sweep no reduction process occurs and that the faradaic processes are inhibited in the second cycle (thick line); the solution turns yellowish, which suggests that a fraction

of the complex anion $[Fe(CN)_6]^{3-}$ partially decomposes during electrochemical experiments.

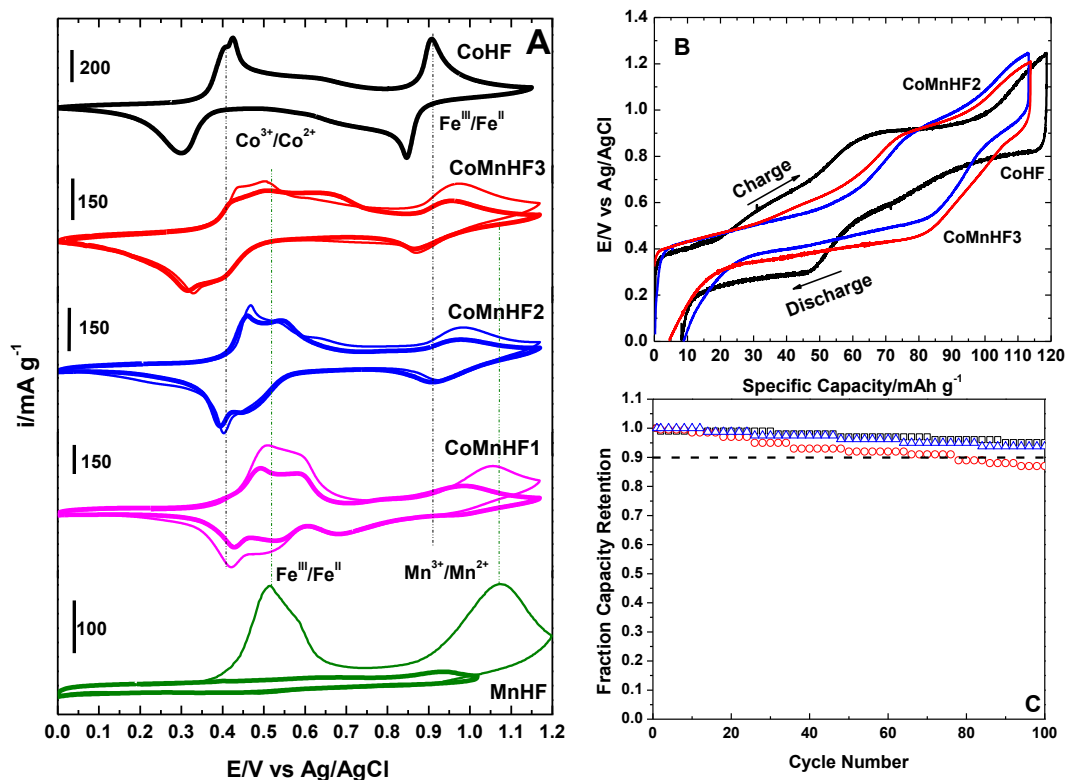Figure 32. A) Cyclic Voltammetry at 1 mV s^{-1} where thin line is 1st cycle and tick line is 2nd cycle for MnHF, 20th cycle for CoMnHF1, 40th cycle for CoMnHF2 and 45th cycle for CoMnHF3; B) Galvanostatic experiment at 1C and C) Fraction Capacity Retention at different cycles.

The samples CoMnHF1, CoMnHF2 and CoMn3 in general the electrochemical profiles exhibited two faradic process at low potential <0.7 V vs Ag/AgCl and at high potential >0.7 V vs Ag/AgCl, for CoMn3 whit a Mn:Co ratio is 1:2, there are not a well-defined peak in the oxidation of process 1 indicating an increment in rearrangement of the electronic structure due to the presence of Co^{3+} (LS), whereas the electrochemical reversibility in redox process 2 decrease (ΔE_p= 88 mV) suggesting that not only Fe(LS) participate in the

faradaic process due to Manganese contribution, this is verify in CoMnHF1 (Mn:Co ratio is 2:1), where the faradic process to high potential is irreversible because the some Mn^{3+} are produce is this process, decreasing the stability, so the current in the 10th decrease (thick line), in this sample the process 1 exhibited two well-defined contributions at E_f = 0.46 and 0.55 V vs Ag/AgCl whit a separation of 100 mV, this is associated to crystalline phases changes from rhombohedral to cubic due to that this material show a higher distortion in unit cell as was discusses before in Raman and Mossbauer results; on the other hand, the CoMnHF2 with an equivalent ratio between Mn:Co, showed a better electrochemical reversibility indicating a fast reaction kinetics (which decrease the energy losses in the battery) and a shift E_f to cathodic potential for both redox process, with a lower (80 mV) separation between the peaks assigned to structural changes (process 1) due to the unit cell presents a lower distortion than CoMnHF1. The proposed mechanism will be discussed later in *in-situ* infrared.

The charge/discharge experiments at 1C (60 mA g^{-1}) for CoHF, CoMnHF3 and CoMnHF2 which exhibited less loss of current for several cycles 50, 45 and 40 (thick line) respectively, are exhibited in Figure 32B. The smooth S-curves type which is associated to solid solution reactions during insertion/desertion of sodium[33], the energy spent during charge is slightly higher than that delivered during discharge. This energy difference is the source of the potential gap between the charge and discharge curves (overpotential). The CoMnHF materials showed two defined plateaus at 0.4-0.66 V vs Ag/AgCl whit an overpotential (calculated as the difference between the average charge and discharge voltages) of 0.1344 V for CoMnHF2 and 0.165 V for CoMnHF3; and 0.9-1.0 V vs Ag/AgCl

with an overpotential of 0.2536 V and 0.4508 V for CoMnHF2 and CoMnHF3 respectively, an increment in overpotential in process one and two is observed in CoHF, this energy difference, can be assigned to ability of $Fe^{III}(LS)$ to accept electrons lower energy states filling the t_{2g} levels followed by an energy decrease and phase stabilization, this phenomena decrease by the presence of Mn in the lattice due to a their lower capacity of charge subtraction over Fe trough cyanide linker. The specific capacity in descending order is 118.81 mAh g^{-1} for CoHF > 113.84 mAh g^{-1} for MnCoHF3 > 112.82 mAh g^{-1} for MnCoHF1, the capacity retention after 100 cycles is 95%, 93% and 87% for CoHF, CoMnHF2 and CoMnHF3 respectively (Fig. 32C).

As was show before the presence of Mn produces an instability in the structure due to during redox process only the electron in e_g orbitals are involve, in particular when the Mn^{3+} is producer promotes strong short-range interactions with the adjacent N atoms due to the orientation of the orbitals along the bond inducing the strain in the framework; whereas the stability exhibited in CoMnHF2 can be assigned to a decrease in the interaction between spin delocalization of Fe center with e_g orbitals of Mn decreasing the Jean Teller distortion by the strong interaction that Cobalt showed in the structure.

4.1.3 In-situ Study

The *In-situ* infrared during charge/discharge process in CoMnHF2 are showed in Figure 33. The IR band attributed to $Fe^{III}(LS)$ appears until 0.6 V vs Ag/AgCl where the second faradic process start, suggesting that the interaction between cobalt and manganese though the spin delocalization of Fe center inhibits the electron transfer from Fe to Mn due to the

Cobalt in the structure exhibited a higher charge subtraction; this can be verify because at 1.0 V vs Ag/AgCl the signal at 2075 cm^{-1} decrease indicating that Fe^{II} disappear which increase during sodium insertion at 0.4 vs Ag/AgCl. Is interesting that no spontaneous electron transfer from Fe^{II} to Mn^{3+} is observed, so that the manganese oxidation takes place a high potential, help to cathode stability.
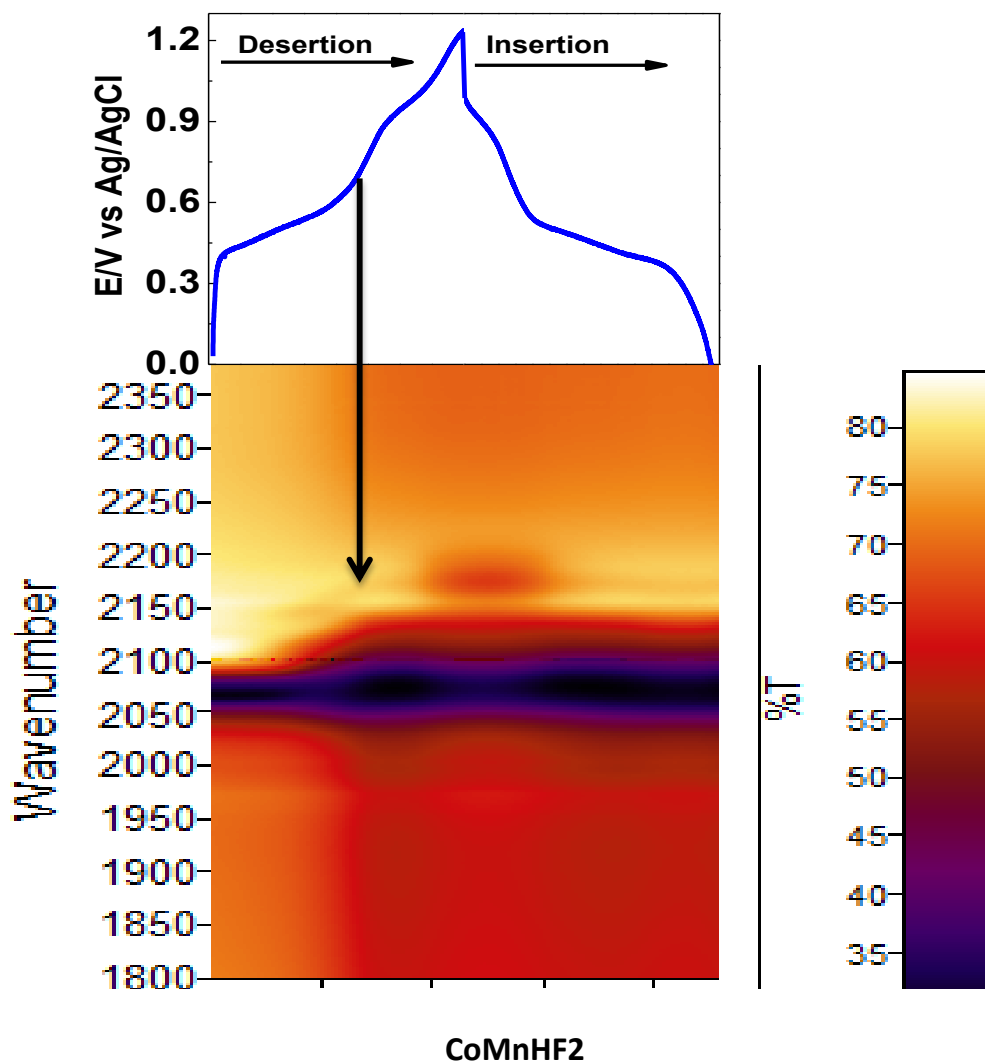

CoMnHF2

Figure 33. *In-situ* Infrared spectroscopy during charge/discharge process.

2.4 Non-aqueous media

In non-aqueous media the $Na_{2y}Mn_x[Fe(CN)_6]_y$ also exhibited the instability in charge/discharge process due to Jahn Teller distortion[67]. In this context the synthesis of Manganese Hexacyanoferrate doped with $3d$ transition metal was proposed; relating the electrochemical behavior to its electronic properties[76].

2.4.1 Structural Characterization

The chemical composition calculated by OES-ICP of every sample and their labeled is exhibited in Table 8.

Table 8. Chemical Composition

Sample	Formula
MnNiHF	$Na_{1.94}Ni_{0.57}Mn_{0.43}[Fe(CN)_6]_{0.97} \cdot 1.93\ H_2O$
MnCoHF	$Na_{1.92}Co_{0.55}Mn_{0.45}[Fe(CN)_6]_{0.96} \cdot 2.03\ H_2O$
MnFeHF	$Na_{1.90}Fe_{0.54}Mn_{0.46}[Fe(CN)_6]_{0.935} \cdot 2.15\ H_2O$
MnHF	$Na_{1.96}Mn[Fe(CN)_6]_{0.98} \cdot 2.21 H_2O$

The X-Ray pattern of MnHF, MnCoHF and MnNiHF, exhibited in Figure 34 reveals a good peaks splitting at 2θ= 24.5°, 38.8°, 49.5° and 55.93° corresponding to the (220), (420), (440) and (620) planes of the cubic crystalline respectively, indicates that materials crystallized in monoclinic lattice with the $P2_1/n$ space group as has been reported
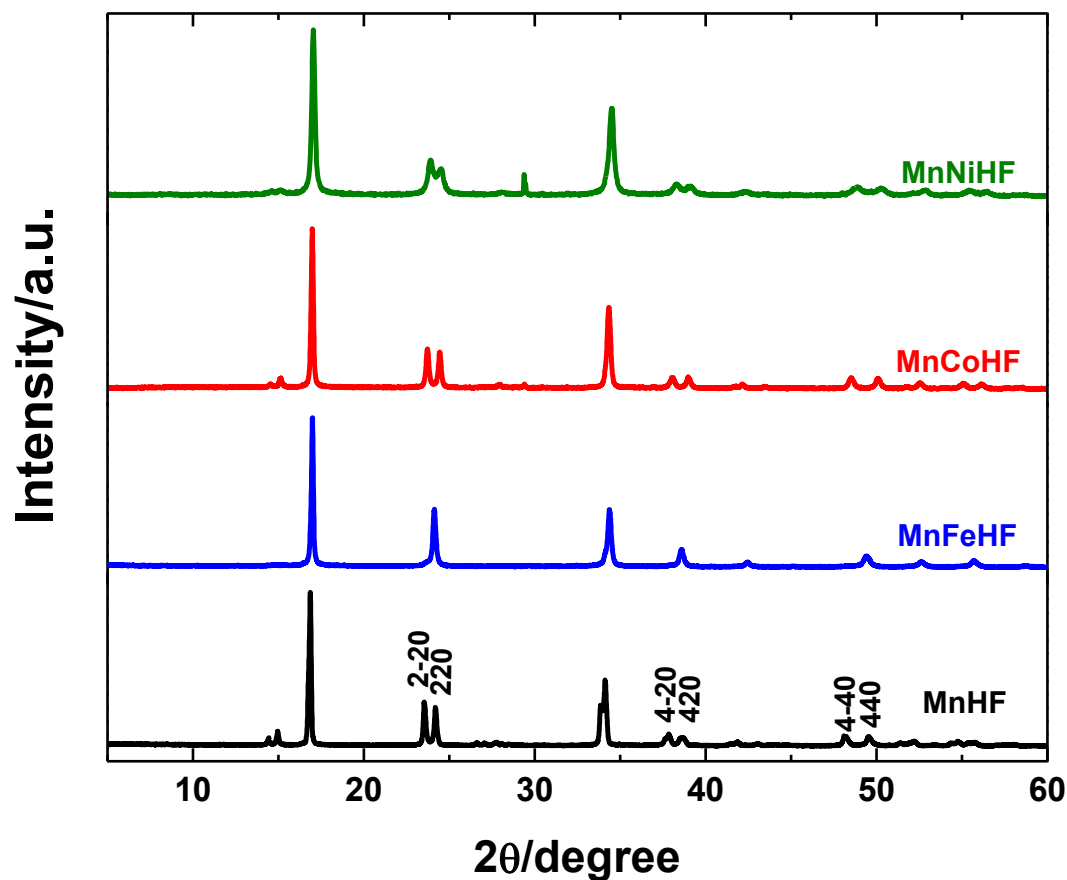
Figure 34. X-Ray Diffraction of MnMHF.

The Infrared spectrum of MnHF (Figure 35) present the vibration band assigned to ν(CN) stretching vibration at 2064 cm^{-1}, suggesting that cation in frameworks has a oxidation state of 2+ in the chain Mn^{2+}-C≡N-Fe^{II}; a shift to higher wave numbers is observed in MnCoHF and MnNiHF, indicating that the partial incorporation of Co (Z/r^2= 3.652) and Ni (Z/r^2= 3.858) in the structure increase the electron subtraction thought cyanide, due to

high polarizing power (Z/r^2).   On the other hand, although Fe^{2+} has a Z/r^2 (3.463) greater than Mn^{2+} (3.287), the IR vibration not change, this can be associated to different crystalline unit cell where in MnFeHF has a symmetrical environment in the octahedral, whereas in the MnHF The axial bond of the octahedron are longer than the equatorial.
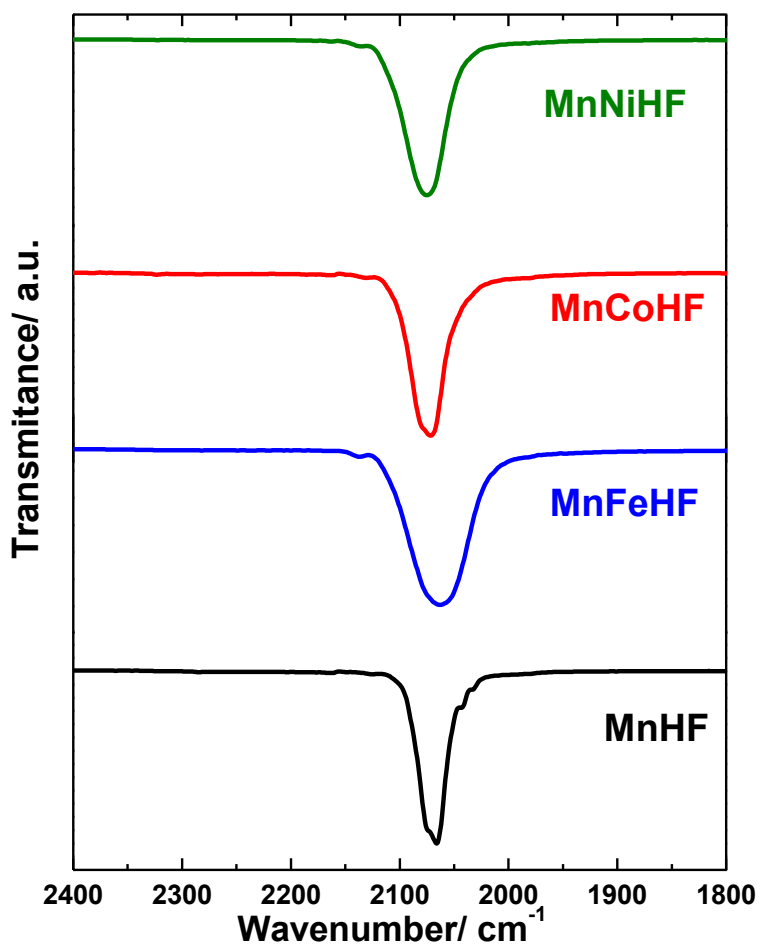

Figure 35. Infrared Spectroscopy

4.2.2. Galvanostatic Experiment

The galvanostatic experiments at 0.1C are exhibited in Figure 36A, during charge the MnHF has one plateau between 3.4-3.7 V vs Na^+/Na, reach a specific capacity of 120 mAh g^{-1}, but during discharge process only can reach 105 mAh g^{-1}, indicating that not all redox sites involves during oxidation process can be reduced in the structure again during reduction process, this can be associated to redox couple Mn^{3+}/Mn^{2+} not have a good reversibility due to pronounced difference in ionic radii for HS Mn^{3+}(0.970 Å) and HS Mn^{2+} (0.785 Å) associated to Jean Teller effect, inducing a distortion in the octahedral MnN_6 where the axial links grow and the equatorial ones decrease due to the, causing that during sodium insertion not all Mn^{3+} can produces Mn^{2+}; this phenomena is more evident with respect to cycle number increase provokes that at 30 cycles the fraction capacity retention decrease at 0.8 at more cycles a large decrease in retention capacity is observed (Figure 36B) indicating a possible segregation phase take place as has been reported before.
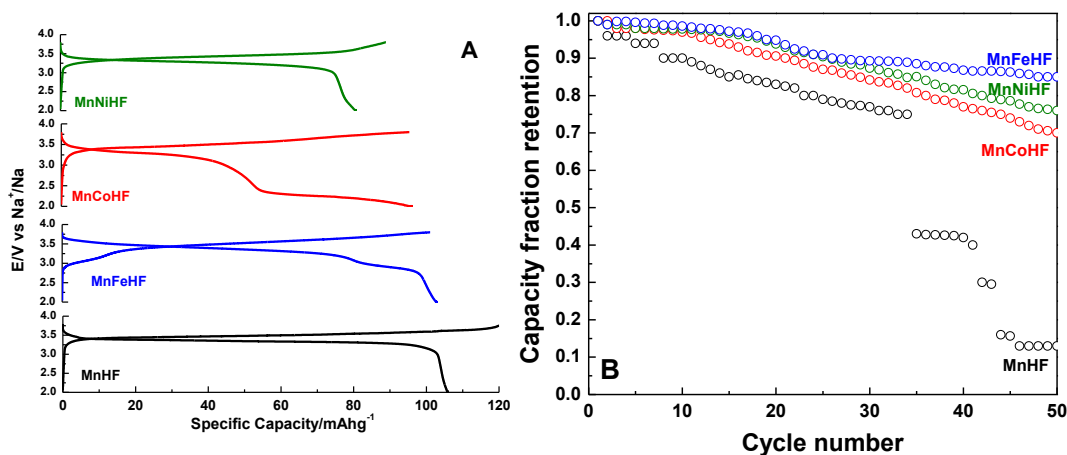

Figure 36. A) Galvanostatic behavior and B) Capacity fraction retention at different cycles.

The effect of partial substitution of Mn for Co, Ni and Fe, shows different electrochemical profiles, the MnCoHF exhibited a plateau during desodiation between 3.3-3.7 V vs Na^+/Na, but during sodiation two plateaus are observed the first between 3.7-3.05 V vs Na^+/Na and second between 2.3-2.0 V vs Na^+/Na, the specific capacity is 95 mAh g^{-1}; whereas the MnNiHF presented the lowest specific capacity 80 mAh g^{-1}, a plateau in charge process are between 3.26-3.54 V vs Na^+/Na and between 3.40-3.0 V vs Na^+/Na during discharge. On the other hand, MnFeHF has a small plateau between 3.0-3.15 V vs Na^+/Na follow by plateau 3.37-3.78 V vs Na^+/Na in sodium desertion and 3.65-3.21 V vs Na^+/Na and 2.96-2.78 V vs Na^+/Na in sodium insertion. The three metals show a stability improvement in the following order Ni < Co < Fe, which is contrary to polarizing power suggesting that charge substation modulate the electron density in Mn decrease the Jean Teller effect during electrochemical process.

4.2 Conclusions

The Jahn Teller effect on Mn^{3+} can be modulated by doping with a 3d metal as outer cation. This modulation is due to the interaction between outer cation in the structure due to the spin delocalization and to charge subtraction due to polarizing power, increasing the charge retention during charge/discharge cycles.

For aqueous media the materials crystallized in monoclinic cell, this distortion in framework is due to high amount of sodium and a low defect in the cell, the different Mn/Co ratio exhibited a different magnetic interaction associated to cation arrangement,

the ratio=1 increase the spin contribution assigned to change from antiferromagnetic to ferromagnetic behavior in the cobalt. This interaction modulated the Jean Teller effect present during oxidation process and inhibits the spontaneous electron transition from Fe^{II} to Mn^{3+} and stabilized the framework during charge/discharge process.

On the other hand, in non-aqueous media the material MnHF, MnCoHF and MnNiHF crystalized in monoclinic cell whereas, the MnFeHF crystallized in cubic cell, the charge subtraction thought the cyanide linker is in function their polarizing power in next order Ni > Co > Fe; the electrochemical results revels that stability in the structure Follows the inverse sense of the polarizing power of the cation 3d.

5. Reference

1.   Dunn, B.; Kamath, H.; Tarascon, J.-M., Electrical Energy Storage for the Grid: A Battery of Choices. *Science* **2011,** *334* (6058), 928-935.

2.   Yang, Z.; Zhang, J.; Kintner-Meyer, M. C. W.; Lu, X.; Choi, D.; Lemmon, J. P.; Liu, J., Electrochemical Energy Storage for Green Grid. *Chemical Reviews* **2011,** *111* (5), 3577-3613.

3.   Grey, C. P.; Tarascon, J. M., Sustainability and in situ monitoring in battery development. *Nat Mater* **2017,** *16* (1), 45-56.

4.   Hwang, J.-Y.; Myung, S.-T.; Sun, Y.-K., Sodium-ion batteries: present and future. *Chemical Society Reviews* **2017**.

5.   Ellis, B. L.; Nazar, L. F., Sodium and sodium-ion energy storage batteries. *Current Opinion in Solid State and Materials Science* **2012,** *16* (4), 168-177.

6.   Kim, H.; Hong, J.; Park, K.-Y.; Kim, H.; Kim, S.-W.; Kang, K., Aqueous Rechargeable Li and Na Ion Batteries. *Chemical Reviews* **2014,** *114* (23), 11788-11827.

7.   Pan, H.; Hu, Y.-S.; Chen, L., Room-temperature stationary sodium-ion batteries for large-scale electric energy storage. *Energy & Environmental Science* **2013,** *6* (8), 2338-2360.

8.   Tarascon, J.-M., Is lithium the new gold? *Nat Chem* **2010,** *2* (6), 510-510.

9.   Goodenough, J. B., Evolution of Strategies for Modern Rechargeable Batteries. *Accounts of Chemical Research* **2013,** *46* (5), 1053-1061.

10.   Kim, H.; Kim, H.; Ding, Z.; Lee, M. H.; Lim, K.; Yoon, G.; Kang, K., Recent Progress in Electrode Materials for Sodium-Ion Batteries. *Advanced Energy Materials* **2016,** *6* (19), 1600943-n/a.

11.   Kim, S.-W.; Seo, D.-H.; Ma, X.; Ceder, G.; Kang, K., Electrode Materials for Rechargeable Sodium-Ion Batteries: Potential Alternatives to Current Lithium-Ion Batteries. *Advanced Energy Materials* **2012,** *2* (7), 710-721.

12.   Yabuuchi, N.; Kubota, K.; Dahbi, M.; Komaba, S., Research Development on Sodium-Ion Batteries. *Chemical Reviews* **2014,** *114* (23), 11636-11682.

13.   Palomares, V.; Casas-Cabanas, M.; Castillo-Martinez, E.; Han, M. H.; Rojo, T., Update on Na-based battery materials. A growing research path. *Energy & Environmental Science* **2013,** *6* (8), 2312-2337.

14.   Ong, S. P.; Chevrier, V. L.; Hautier, G.; Jain, A.; Moore, C.; Kim, S.; Ma, X.; Ceder, G., Voltage, stability and diffusion barrier differences between sodium-ion and lithium-ion intercalation materials. *Energy & Environmental Science* **2011,** *4* (9), 3680-3688.

15.   (a) Fu, S.; Ni, J.; Xu, Y.; Zhang, Q.; Li, L., Hydrogenation Driven Conductive Na2Ti3O7 Nanoarrays as Robust Binder-Free Anodes for Sodium-Ion Batteries. *Nano Letters* **2016,** *16* (7), 4544-4551; (b) Wang, B.; Zhao, F.; Du, G.; Porter, S.; Liu, Y.; Zhang, P.; Cheng, Z.; Liu, H. K.; Huang, Z., Boron-Doped Anatase TiO2 as a High-Performance Anode Material for Sodium-Ion Batteries. *ACS Applied Materials & Interfaces* **2016,** *8* (25), 16009-16015.

16.   Putungan, D. B.; Lin, S.-H.; Kuo, J.-L., Metallic VS2 Monolayer Polytypes as Potential Sodium-Ion Battery Anode via ab Initio Random Structure Searching. *ACS Applied Materials & Interfaces* **2016,** *8* (29), 18754-18762.

17.   Cui, J.; Xu, Z.-L.; Yao, S.; Huang, J.; Huang, J.-Q.; Abouali, S.; Garakani, M. A.; Ning, X.; Kim, J.-K., Enhanced conversion reaction kinetics in low crystallinity SnO2/CNT anodes for Na-ion batteries. *Journal of Materials Chemistry A* **2016,** *4* (28), 10964-10973.

18.   Li, Z.; Ma, L.; Surta, T. W.; Bommier, C.; Jian, Z.; Xing, Z.; Stickle, W. F.; Dolgos, M.; Amine, K.; Lu, J.; Wu, T.; Ji, X., High Capacity of Hard Carbon Anode in Na-Ion Batteries Unlocked by POx Doping. *ACS Energy Letters* **2016,** *1* (2), 395-401.

19.   Su, H.; Jaffer, S.; Yu, H., Transition metal oxides for sodium-ion batteries. *Energy Storage Materials* **2016,** *5*, 116-131.

20.   Liu, H.; Xu, J.; Ma, C.; Meng, Y. S., A new O3-type layered oxide cathode with high energy/power density for rechargeable Na batteries. *Chemical Communications* **2015,** *51* (22), 4693-4696.

21.   Li, H.; Wu, C.; Bai, Y.; Wu, F.; Wang, M., Controllable synthesis of high-rate and long cycle-life Na3V2(PO4)3 for sodium-ion batteries. *Journal of Power Sources* **2016,** *326*, 14-22.

22.   Noguchi, Y.; Kobayashi, E.; Plashnitsa, L. S.; Okada, S.; Yamaki, J.-i., Fabrication and performances of all solid-state symmetric sodium battery based on NASICON-related compounds. *Electrochimica Acta* **2013,** *101*, 59-65.

23.   Li, C.; Miao, X.; Chu, W.; Wu, P.; Tong, D. G., Hollow amorphous NaFePO4 nanospheres as a high-capacity and high-rate cathode for sodium-ion batteries. *Journal of Materials Chemistry A* **2015,** *3* (16), 8265-8271.

24.   Chihara, K.; Kubota, K.; Komaba, S., Na2CoPO4f As High Voltage Positive Materials for Sodium Ion Batteries. *Meeting Abstracts* **2015,** *MA2015-02* (3), 232.

25.   Lu, Y.; Wang, L.; Cheng, J.; Goodenough, J. B., Prussian blue: a new framework of electrode materials for sodium batteries. *Chemical Communications* **2012,** *48* (52), 6544-6546.

26.   Balmaseda, J.; Reguera, E.; Rodríguez-Hernández, J.; Reguera, L.; Autie, M., Behavior of transition metals ferricyanides as microporous materials. *Microporous and Mesoporous Materials* **2006,** *96* (1–3), 222-236.

27.   Tokoro, H.; Ohkoshi, S.-i., Novel magnetic functionalities of Prussian blue analogs. *Dalton Transactions* **2011,** *40* (26), 6825-6833.

28.   Ohkoshi, S.-i.; Nakagawa, K.; Tomono, K.; Imoto, K.; Tsunobuchi, Y.; Tokoro, H., High Proton Conductivity in Prussian Blue Analogues and the Interference Effect by Magnetic Ordering. *Journal of the American Chemical Society* **2010,** *132* (19), 6620-6621.

29.   García-Ortiz, A.; Grirrane, A.; Reguera, E.; García, H., Mixed (Fe2+ and Cu2+) double metal hexacyanocobaltates as solid catalyst for the aerobic oxidation of oximes to carbonyl compounds. *Journal of Catalysis* **2014,** *311*, 386-392.

30.   Reguera, L.; Balmaseda, J.; del Castillo, L. F.; Reguera, E., Hydrogen Storage in Porous Cyanometalates: Role of the Exchangeable Alkali Metal. *The Journal of Physical Chemistry C* **2008,** *112* (14), 5589-5597.

31.   Fernández-Ropero, A. J.; Piernas-Muñoz, M. J.; Castillo-Martínez, E.; Rojo, T.; Casas-Cabanas, M., Electrochemical characterization of NaFe2(CN)6 Prussian Blue as positive electrode for aqueous sodium-ion batteries. *Electrochimica Acta* **2016,** *210*, 352-357.

32.   Sinha, S.; Humphrey, B. D.; Bocarsly, A. B., Reaction of nickel electrode surfaces with anionic metal-cyanide complexes: formation of precipitated surfaces. *Inorganic Chemistry* **1984,** *23* (2), 203-212.

33.   Wessells, C. D.; Peddada, S. V.; McDowell, M. T.; Huggins, R. A.; Cui, Y., The Effect of Insertion Species on Nanostructured Open Framework Hexacyanoferrate Battery Electrodes. *Journal of The Electrochemical Society* **2011,** *159* (2), A98-A103.

34.   Wessells, C. D.; Peddada, S. V.; Huggins, R. A.; Cui, Y., Nickel Hexacyanoferrate Nanoparticle Electrodes For Aqueous Sodium and Potassium Ion Batteries. *Nano Letters* **2011,** *11* (12), 5421-5425.

35.   Wessells, C. D.; Huggins, R. A.; Cui, Y., Copper hexacyanoferrate battery electrodes with long cycle life and high power. *Nature Communications* **2011,** *2*, 550.

36.   Wessells, C. D.; McDowell, M. T.; Peddada, S. V.; Pasta, M.; Huggins, R. A.; Cui, Y., Tunable Reaction Potentials in Open Framework Nanoparticle Battery Electrodes for Grid-Scale Energy Storage. *ACS Nano* **2012,** *6* (2), 1688-1694.

37.   Hung, T.-F.; Chou, H.-L.; Yeh, Y.-W.; Chang, W.-S.; Yang, C.-C., Combined Experimental and Computational Studies of a Na2Ni1–xCuxFe(CN)6 Cathode with Tunable Potential for Aqueous Rechargeable Sodium-Ion Batteries. *Chemistry – A European Journal* **2015,** *21* (44), 15686-15691.

38.   Wu, X.-y.; Sun, M.-y.; Shen, Y.-f.; Qian, J.-f.; Cao, Y.-l.; Ai, X.-p.; Yang, H.-x., Energetic Aqueous Rechargeable Sodium-Ion Battery Based on Na2CuFe(CN)6–NaTi2(PO4)3 Intercalation Chemistry. *ChemSusChem* **2014,** *7* (2), 407-411.

39.   Wu, X.; Sun, M.; Guo, S.; Qian, J.; Liu, Y.; Cao, Y.; Ai, X.; Yang, H., Vacancy-Free Prussian Blue Nanocrystals with High Capacity and Superior Cyclability for Aqueous Sodium-Ion Batteries. *ChemNanoMat* **2015,** *1* (3), 188-193.

40.   Wu, X.; Luo, Y.; Sun, M.; Qian, J.; Cao, Y.; Ai, X.; Yang, H., Low-defect Prussian blue nanocubes as high capacity and long life cathodes for aqueous Na-ion batteries. *Nano Energy* **2015,** *13*, 117-123.

41.   Lee, J.-H.; Ali, G.; Kim, D. H.; Chung, K. Y., Metal-Organic Framework Cathodes Based on a Vanadium Hexacyanoferrate Prussian Blue Analogue for High-Performance Aqueous Rechargeable Batteries. *Advanced Energy Materials* **2017,** *7* (2), 1601491-n/a.

42.   (a) You, Y.; Wu, X.-L.; Yin, Y.-X.; Guo, Y.-G., High-quality Prussian blue crystals as superior cathode materials for room-temperature sodium-ion batteries. *Energy & Environmental Science* **2014,** *7* (5), 1643-1647; (b) Wang, L.; Lu, Y.; Liu, J.; Xu, M.; Cheng, J.; Zhang, D.; Goodenough, J. B., A Superior Low-Cost Cathode for a Na-Ion Battery. *Angewandte Chemie International Edition* **2013,** *52* (7), 1964-1967; (c) You, Y.; Yu, X.; Yin, Y.; Nam, K.-W.; Guo, Y.-G., Sodium iron hexacyanoferrate with high Na content as a Na-rich cathode material for Na-ion batteries. *Nano Research* **2015,** *8* (1), 117-128.

43.   (a) Yu, S.; Li, Y.; Lu, Y.; Xu, B.; Wang, Q.; Yan, M.; Jiang, Y., A promising cathode material of sodium iron–nickel hexacyanoferrate for sodium ion batteries. *Journal of Power Sources* **2015,** *275*, 45-49; (b) Yang, D.; Xu, J.; Liao, X.-Z.; He, Y.-S.; Liu, H.; Ma, Z.-F., Structure optimization of Prussian blue analogue cathode materials for advanced sodium ion batteries. *Chemical Communications* **2014,** *50* (87), 13377-13380; (c) Xie, M.; Xu, M.; Huang, Y.; Chen, R.; Zhang, X.; Li, L.; Wu, F., Na2NixCo1 − xFe(CN)6: A class of Prussian blue analogs with transition metal elements as cathode materials for sodium ion batteries. *Electrochemistry Communications* **2015,** *59*, 91-94.

44.   (a) Wan, M.; Tang, Y.; Wang, L.; Xiang, X.; Li, X.; Chen, K.; Xue, L.; Zhang, W.; Huang, Y., Core-shell hexacyanoferrate for superior Na-ion batteries. *Journal of Power Sources* **2016,** *329*, 290-296; (b) Okubo, M.; Li, C. H.; Talham, D. R., High rate sodium ion insertion into core-shell nanoparticles of Prussian blue analogues. *Chemical Communications* **2014,** *50* (11), 1353-1355.

45.   Wu, X.; Wu, C.; Wei, C.; Hu, L.; Qian, J.; Cao, Y.; Ai, X.; Wang, J.; Yang, H., Highly Crystallized Na2CoFe(CN)6 with Suppressed Lattice Defects as Superior Cathode Material for Sodium-Ion Batteries. *ACS Applied Materials & Interfaces* **2016,** *8* (8), 5393-5399.

46.   Song, J.; Wang, L.; Lu, Y.; Liu, J.; Guo, B.; Xiao, P.; Lee, J.-J.; Yang, X.-Q.; Henkelman, G.; Goodenough, J. B., Removal of Interstitial H2O in Hexacyanometallates for a Superior Cathode of a Sodium-Ion Battery. *Journal of the American Chemical Society* **2015,** *137* (7), 2658-2664.

47.   Oliver-Tolentino, M. A.; Vazquez-Samperio, J.; Cabrera-Sierra, R.; Reguera, E., Materials for aqueous sodium-ion batteries: cation mobility in a zinc hexacyanoferrate electrode. *RSC Advances* **2016,** *6* (110), 108627-108634.

48.   Lee, H.; Kim, Y.-I.; Park, J.-K.; Choi, J. W., Sodium zinc hexacyanoferrate with a well-defined open framework as a positive electrode for sodium ion batteries. *Chemical Communications* **2012,** *48* (67), 8416-8418.

49.   Ni, G.; Han, B.; Li, Q.; Ji, Z.; Huang, B.; Zhou, C., Instability of Zinc Hexacyanoferrate Electrode in an Aqueous Environment: Redox-Induced Phase Transition, Compound Dissolution, and Inhibition. *ChemElectroChem* **2016,** *3* (5), 798-804.

50.   Avila, M.; Rodríguez-Hernández, J.; Lemus-Santana, A. A.; Reguera, E., Cation mobility and structural changes on the water removal in zeolite-like zinc hexacyanometallates (II). *Journal of Physics and Chemistry of Solids* **2011,** *72* (8), 988-993.

51.   Perez-Cappe, E.; Aguilar-Frutis, M.; Chavez, N.; Ribalta, J.; Reguera, E., Cation mobility in a series of zeolite-like coordination polymers. *Microporous and Mesoporous Materials* **2012,** *163*, 326-333.

52.   Scholz, F.; Dostal, A., The Formal Potentials of Solid Metal Hexacyanometalates. *Angewandte Chemie International Edition in English* **1996,** *34* (23-24), 2685-2687.

53.   Boukamp, B. A., A Nonlinear Least Squares Fit procedure for analysis of immittance data of electrochemical systems. *Solid State Ionics* **1986,** *20* (1), 31-44.

54.   Yang, D.; Xu, J.; Liao, X.-Z.; Wang, H.; He, Y.-S.; Ma, Z.-F., Prussian blue without coordinated water as a superior cathode for sodium-ion batteries. *Chemical Communications* **2015,** *51* (38), 8181-8184.

55.   (a) Liu, C.; Neale, Z. G.; Cao, G., Understanding electrochemical potentials of cathode materials in rechargeable batteries. *Materials Today* **2016,** *19* (2), 109-123; (b) Goodenough, J. B.; Park, K.-S., The Li-Ion Rechargeable Battery: A Perspective. *Journal of the American Chemical Society* **2013,** *135* (4), 1167-1176.

56.   Yamada, A.; Koizumi, H.; Sonoyama, N.; Kanno, R., Phase Change in Li x FePO4. *Electrochemical and Solid-State Letters* **2005,** *8* (8), A409-A413.

57.   Knauth, P., Ionic and electronic conduction in nanostructured solids: Concepts and concerns, consensus and controversies. *Solid State Ionics* **2006,** *177* (26–32), 2495-2502.

58.   Loera-Serna, S.; Oliver-Tolentino, M. A.; de Lourdes López-Núñez, M.; Santana-Cruz, A.; Guzmán-Vargas, A.; Cabrera-Sierra, R.; Beltrán, H. I.; Flores, J., Electrochemical behavior of [Cu3(BTC)2] metal–organic framework: The effect of the method of synthesis. *Journal of Alloys and Compounds* **2012,** *540*, 113-120.

59.   Bueno, P. R.; Giménez-Romero, D.; Ferreira, F. F.; Setti, G. O., Electrochemical capacitance spectroscopy and capacitive relaxation of the changeover process in iron hexacyanoferrate molecular compound. *Electrochimica Acta* **2010,** *55* (21), 6147-6155.

60.   Orikasa, Y.; Maeda, T.; Koyama, Y.; Murayama, H.; Fukuda, K.; Tanida, H.; Arai, H.; Matsubara, E.; Uchimoto, Y.; Ogumi, Z., Transient Phase Change in Two Phase Reaction between LiFePO4 and FePO4 under Battery Operation. *Chemistry of Materials* **2013,** *25* (7), 1032-1039.

61.   Zhu, Y.; Wang, C., Galvanostatic Intermittent Titration Technique for Phase-Transformation Electrodes. *The Journal of Physical Chemistry C* **2010,** *114* (6), 2830-2841.

62.   Lee, H.-W.; Pasta, M.; Wang, R. Y.; Ruffo, R.; Cui, Y., Effect of the alkali insertion ion on the electrochemical properties of nickel hexacyanoferrate electrodes. *Faraday Discussions* **2014,** *176* (0), 69-81.

63.   Marcus, Y., Thermodynamics of solvation of ions. Part 5.-Gibbs free energy of hydration at 298.15 K. *Journal of the Chemical Society, Faraday Transactions* **1991,** *87* (18), 2995-2999.

64.   Shakourian-Fard, M.; Kamath, G.; Smith, K.; Xiong, H.; Sankaranarayanan, S. K. R. S., Trends in Na-Ion Solvation with Alkyl-Carbonate Electrolytes for Sodium-Ion Batteries: Insights from First-Principles Calculations. *The Journal of Physical Chemistry C* **2015,** *119* (40), 22747-22759.

65.   Pasta, M.; Wang, R. Y.; Ruffo, R.; Qiao, R.; Lee, H.-W.; Shyam, B.; Guo, M.; Wang, Y.; Wray, L. A.; Yang, W.; Toney, M. F.; Cui, Y., Manganese-cobalt hexacyanoferrate cathodes for sodium-ion batteries. *Journal of Materials Chemistry A* **2016,** *4* (11), 4211-4223.

66.   Chen, R.; Huang, Y.; Xie, M.; Wang, Z.; Ye, Y.; Li, L.; Wu, F., Chemical Inhibition Method to Synthesize Highly Crystalline Prussian Blue Analogs for Sodium-Ion Battery Cathodes. *ACS Applied Materials & Interfaces* **2016,** *8* (46), 31669-31676.

67.   Sottmann, J.; Bernal, F. L. M.; Yusenko, K. V.; Herrmann, M.; Emerich, H.; Wragg, D. S.; Margadonna, S., In operando Synchrotron XRD/XAS Investigation of Sodium Insertion into the Prussian Blue Analogue Cathode Material Na1.32Mn[Fe(CN)6]0.83·z H2O. *Electrochimica Acta* **2016,** *200*, 305-313.

68.   Bertrán, J. F.; Pascual, J. B.; Ruiz, E. R., The CN stretch of hexacyanometallates as a sensor of ligand—outer cation interactions—I. Ferricyanides and cobalticyanides. *Spectrochimica Acta Part A: Molecular Spectroscopy* **1990,** *46* (5), 685-689.

69.   Ojwang, D. O.; Grins, J.; Wardecki, D.; Valvo, M.; Renman, V.; Häggström, L.; Ericsson, T.; Gustafsson, T.; Mahmoud, A.; Hermann, R. P.; Svensson, G., Structure Characterization and Properties of K-Containing Copper Hexacyanoferrate. *Inorganic Chemistry* **2016,** *55* (12), 5924-5934.

70.   (a) Samain, L.; Gilbert, B.; Grandjean, F.; Long, G. J.; Strivay, D., Redox reactions in Prussian blue containing paint layers as a result of light exposure. *Journal of Analytical Atomic Spectrometry* **2013,** *28* (4), 524-535; (b) Gómez, A.; Reguera, E., The structure of three cadmium hexacyanometallates(II): Cd2[Fe(CN)6]·8H2O, Cd2[Ru(CN)6]·8H2O and Cd2[Os(CN)6]·8H2O. *International Journal of Inorganic Materials* **2001,** *3* (7), 1045-1051.

71.   Fernández-Bertrán, J.; Reguera, E.; Dago, A.; López-Hernández, C.; Infante, G., Synthesis and characterization of two complexes of glycine with lanthanum hexacyanoferrate(III) and hexacyanocobaltate(III). *Polyhedron* **1996,** *15* (2), 315-319.

72.   Reguera, E.; Fernández-Bertrán, J., Effect of the water of crystallization on the Mössbauer spectra of hexacyanoferrates (II and III). *Hyperfine Interactions* **1994,** *88* (1), 49-58.

73.   Manzan, R. S.; Donoso, J. P.; Magon, C. J.; Silva, I. d. A. A.; Rüssel, C.; Nalin, M., Optical and Structural Studies of Mn2+ Doped SbPO4-ZnO-PbO Glasses. *Journal of the Brazilian Chemical Society* **2015,** *26*, 2607-2614.

74.   Ohkoshi, S.-i.; Iyoda, T.; Fujishima, A.; Hashimoto, K., Magnetic properties of mixed ferro-ferrimagnets composed of Prussian blue analogs. *Physical Review B* **1997,** *56* (18), 11642-11652.

75.   Mayoh, B.; Day, P., Charge transfer in mixed-valence solids. Part VIII. Contribution of valence delocalisation to the ferromagnetism of Prussian Blue. *Journal of the Chemical Society, Dalton Transactions* **1976,** (15), 1483-1486.

76.   Moritomo, Y.; Urase, S.; Shibata, T., Enhanced battery performance in manganese hexacyanoferrate by partial substitution. *Electrochimica Acta* **2016,** *210*, 963-969.